8 X-Ray Absorption Spectroscopy of the Micas

Annibale Mottana[1,2], Augusto Marcelli[2], Giannantonio Cibin[2], and M. Darby Dyar[3]

[1] *Università degli Studi Roma Tre, Dipartimento di Scienze Geologiche Largo S. Leonardo Murialdo 1, I-00146 Roma RM, Italy*

[2] *Istituto Nazionale di Fisica Nucleare, Laboratori Nazionali di Frascati Via Enrico Fermi 40, I-00044 Frascati RM, Italy*

[3] *Mount Holyoke College, Department of Earth and Environment 50 College Street, South Hadley, Massachusetts 01075*

mottana@uniroma3.it

INTRODUCTION

X-ray absorption spectroscopy (XAS) has developed into a powerful tool for the study of all types of materials since the early 1970s, when strong sources such as synchrotrons became available from which experimental spectra with high signal to noise ratios and fine spectral details could be recorded. Just a little earlier, some physical theories had been conceived to explain the XAS spectra, which until then had been recorded using conventional X-ray sources (Sayers et al. 1970, 1971; Stern 1974; Lee and Pendry 1975; Pendry 1983). As soon as new, well-resolved experimental data became available, those theories developed into practical methods by which XAS spectra could be numerically computed and theoretically understood (Kutzler et al. 1980; Natoli et al. 1980; Durham et al. 1982; Natoli et al. 1990; Filipponi et al. 1991; Rehr et al. 1992; Tyson et al. 1992; Zabinsky et al. 1995; Filipponi and Di Cicco 2000; see Rehr and Albers 2000 for a recent review). At present, a full range of applications in material science makes routine use of XAS, and numerous reviews have been published that highlight its potentials in all fields of modern research (e.g., Stern and Heald 1983; Teo 1986; Bianconi 1988; Gurman 1989; Lytle 1989; Henderson et al. 1991).

Specifically for mineral science, XAS became definitively established in the middle 1980s, after a period of parasitical development during which the technical and theoretical principles of the method were adapted and finalized to all types of Earth materials: the crystalline ones, mostly, as well as those in the glassy state (cf. Brown et al. 1978; Calas et al. 1980, 1984; Waychunas et al. 1983, 1986; Davoli et al. 1987, 1988; Brown and Parks 1989; Bassett and Brown 1990; see Brown et al. 1988, 1995 for reviews).

Currently, the main advantages of synchrotron-activated XAS in mineral studies can be outlined as follows:

(a) XAS is element-specific, and can be used for multi-atomic compounds (most natural minerals) with no loss of information on any individual atom, the concentration of which in the sample may range from 100 wt % as in a pure element down to few parts per million (ppm) as in a very diluted natural mixture.

(b) XAS is a local structural probe: although the sample is irradiated by photons, the physical probe is the excited electron. The mean free path of the photoelectron is system-dependent, but it is small. As a result, the excited electron probes a small cluster around the photo-absorbing site (Müller et al. 1982). In other words, it can detect only a few shells of neighbors around the absorbing atom (typically up to a distance of ca. 0.6~0.9 nm), thus giving information mainly on short-range order that is impossible to gather

1529-6466/02/0046-0008$05.00 doi:10.2138/rmg.2002.46.08

otherwise on either ordered (i.e., crystalline) or disordered (i.e., glassy) systems.

(c) XAS is recorded by means of a brilliant photon beam that is strongly linearly polarized in the plane of the synchrotron ring (in this review we will neglect other polarization states now available in modern storage rings using special insertion devices). Moreover, the beam can be focussed down to very small areas (0.1 × 0.2 μm: microXANES, i.e., SmX: Dyar et al. 2001; <100 nm: Kaulich et al. 2000). Thus, XAS can give information on the local site anisotropy of the material.

(d) XAS is a very fast process, the estimated time of the photon absorption excitation being of the order of 10^{-16} s, so that spectra may easily distinguish physical processes that happen on longer time-scales. Moreover, the availability of brilliant and intense sources now allows collection of XAS spectra with high signal to noise ratios in a short time (<1 s), thus following the dynamics of reaction processes practically in real time on a very short time scale (s to min). The so-called dispersive EXAFS system (Phizackerley et al. 1983; Dartige et al. 1986) has reached the same resolution as that of standard double-crystal monochromators, and opened the field of time-resolved XANES experiments to investigate structural dynamical processes.

(e) Extended XAS (i.e., EXAFS: Extended X-ray Absorption Fine Structure [spectroscopy]) provides average interatomic distances accurate to ±0.002 nm, and average coordination numbers accurate to ±10-20%, at least for the nearest or next-nearest-coordination shells. Polarized X-ray absorption spectra show a strong dichroism for anisotropic sites. Moreover, in the single scattering approximation that best describes polarized EXAFS spectra (i.e., P-EXAFS; cf. Benfatto et al. 1989), oscillations originating at a particular scattered atom can appear or disappear depending on whether or not the electric field is directed towards that atom.

(f) Near-edge XAS (i.e., XANES: X-ray Absorption Near-Edge Structure [spectroscopy]), although not yet fully quantitative, provides high-quality information on oxidation state, symmetry, coordination and bonding of atoms in their local environment; furthermore, it gives some indication of bond distances and angles. While in EXAFS the electron scattering is weak and the observed modulation of the absorption cross-section barely reaches 5% of the total signal, in XANES the electron scattering is much stronger and the modulated signal is significantly larger. Nevertheless, quantitative interpretation of near-edge experiments is never simple: some theoretical help may be obtained from recently developed computer codes (Joly 2001).

(g) XAS can be used as a bulk method to look for information on samples that are very fine-grained (powders), even using impure mixes (provided that the associated material does not contain the atom to be probed in the mineral). Alternatively, it can be used on oriented specimens, provided suitable crystals are available, which can be oriented either crystallographically or morphologically on the sample holder. Using a special set up, XAS can even be used to scan only the surface of a mineral (SEXAFS) or the interface between two contacting layers (e.g., the fresh substrate and its transformation crust). Polarized XAS spectra have been widely used in this context to determine separate interatomic distances on planes parallel and normal to a surface plane. In the XANES spectra of anisotropic clusters the polarization dependence of the absorption cross-section allows the multiple-scattering contributions due to a set of atoms in a particular direction or on a plane to be selectively recorded. Therefore, the orientation and angular distribution of neighboring atoms can be easily determined by changing the relative position between the incident beam and the sample. In angular-resolved XAS spectroscopy, dichroism is usually very large and appears both in the threshold region for the molecular-like bound excitations, producing the white-line, and upwards, all along the spectrum up to the EXAFS region. The interpretation of polarized XANES spectra in terms of multiple-scattering theory allows the role of a selected group

of atoms to be determined. Moreover, the measurement and multiple-scattering interpretation of angular-resolved XANES spectra, when possible, is very useful to unravel and clarify the non-polarized spectrum of the same material.

Because of all these advantages, the number of minerals studied by XAS ranges now over 500, being limited only by their availability (rarity). The number of papers devoted to minerals (including synthetic analogues) making use of XAS exceeds 3000. Nevertheless, there are still problems that limit the usefulness of XAS for certain types of minerals. Among these problems, the most relevant one lies in the morphology of the mineral itself, which usually relates to the anisotropy of its structure. Consequently, minerals such as the phyllosilicates are still among the least studied by XAS: on one side, those usually available as powders (clay minerals) can be best studied, and indeed have been frequently, because XAS provides information unattainable by other methods (e.g., Bonnin et al. 1985; Manceau and Calas 1986; Manceau 1990; Paris et al. 1991); on the other side, and by contrast, for those phyllosilicates that occur as both fine and coarse grains, XAS information might appear to be only complementary, or even superfluous, when compared to the wealth of information gathered by other methods, unless the highly polarized nature of synchrotron radiation is suitably employed (cf. Manceau et al. 1988, 1990, 1998).

The purposes of this review are:

(1) to collect and present the widest possible spectrum of XAS studies performed on the micas, the most common group of phyllosilicates and the one that displays the greatest textural variability: certain species occur only as powders and others may be up to gigantic crystals (e.g., 4.27 × 4.27 × 10.06 m as found at the Lacey Mine, Loughborough Township, Ontario, Canada phlogopite in pegmatite: Rickwood 1981);

(2) to show that studies by XAS on micas must be pursued, because they provide important information unattainable by other methods or, if attainable, certainly more rewarding (though painstaking and time-consuming).

To these purposes, a review of the methods used for the study of lamellar materials will also be included, and indications on how to ameliorate spectral recording to enhance fine details will be given. Nevertheless, we point out that combining XAS with other techniques (e.g., XRD, NMR, neutron scattering, etc.) is still the best way to fully characterize any material at the present time. See Table 1 for definitions of spectroscopic symbols used in this chapter.

OVERVIEW OF THE XAS METHOD

XAS spectroscopy is basically an application of Lambert's law, i.e., a measurement of the variation of *linear X-ray absorption coefficient* μ (defined as $\mu = \mu_m \rho$ [cm^{-1}]) as a function of X-ray *energy* E (defined as $E = h\nu$ [eV]) in the region across the characteristic absorption edge of the atom Z (absorber) to be determined in the investigated material. A modern synchrotron-radiation activated XAS spectrum essentially reports the same structures near and far away the absorption edges as those that were first detected by Hertz (1920) and Fricke (1920) using conventional discharge tubes. However, more details and much greater resolution is now obtained, particularly for the fine structures in the region immediately following the absorption threshold (defined as the energy of the lowest empty state reached by the core excitations). The properties of X-ray absorption edges were explained long ago in their general terms (Kossel 1920; Kronig 1931 1932a,b), but only much later have satisfactory theories been proposed (Sayers et al. 1970; Stern 1974; Lee and Pendry 1975; Dehmer and Dill 1976; see Lytle 1999 for a

Table 1. Definitions of spectroscopic symbols.

Symbol	***Property***
ρ	electron density
h	Planck's constant
ν	photon frequency
k	photoelectron wavenumber
E	photon energy
E_F	Fermi energy
$\sigma(E)$	absorption cross section
M_{if}	matrix element of the electronic transition
δ	Dirac delta function
E_i	energy of the initial state
E_f	energy of the final state
$\Psi_f(r_1, r_2,...., r_n)$	final many-body radial wave function
$\Psi_i(r_1, r_2,...., r_n)$	initial many-body radial wave function
r_n	vector describing the position of the n-th electron
ε	polarization vector of the radiation
α	fine-structure constant
$m_L(\varepsilon)$	matrix element, between the radial part of the wave function calculated inside the sphere of the absorbing atom and the corresponding function of the absorbing atom, which chooses the final angular momentum L
Im	imaginary part
$\mathbb{I}$	unit matrix
l	orbital angular momentum
t_l^i	atomic t-matrix element of the atom at site i
$\mathbb{T}_a = \delta_{ij}\,\delta_{LL'}\,t_l^i$	diagonal matrix of atomic t-matrix elements describing the scattering process (i-j) of the L spherical wave photoelectron
$\mathbb{H} = H^{ij}_{LL'}\,(1-\delta_{ij})$	free amplitude propagator of the photoelectron in the spherical wave state from site i with angular momentum L to site j with angular momentum L'
$M_{l,l\pm1}$	atomic dipole transition matrix element for the photoabsorbing atom (radial part only)
δ_l^0	phase shift of the absorbing atom
α_F	total absorption coefficient
α_0	atomic absorption coefficient
χ_n	the n-th contribution arising from all multiple scattering pathways beginning and ending at the central atom, and involving n-1 neighboring atoms.
$P_l(\cos\phi)$	Legendre polynomials
$f_i(\omega)$	scattering amplitudes of the i-th atom
$R_{tot}= r_i+r_{ij}+r_j$	total length of the triangle composed by the absorbing atom and the i-th and j-th atoms.

historical review). Even more recently a long-lasting attempt has been dedicated to developing a complete and unifying theory for XAS (Natoli 1983; Natoli and Benfatto 1986; see Davoli and Paris 1990, and Rehr and Albers 2000, for reviews).

For theoretical as well as for practical purposes, a XAS spectrum is normally divided in two regions: (1) the X-ray absorption near-edge structure (XANES) region, and (2) the extended X-ray absorption fine structure (EXAFS) region.

EXAFS

In the absorption coefficient formalism, the EXAFS signal is substantially due to interference of the outgoing photoelectron wave from the absorbing atom with the back-scattered wave from each surrounding atom. Hence EXAFS provides information about the pair distribution function.

EXAFS spectra were adequately recorded even at the time when conventional X-ray spectrometers were used, and indeed rotating-anode X-ray sources with brightness in the range 10^8~10^9 photons.s^{-1}.mm^{-2}.$mrad^{-2}$.(0.1% bandwidth)$^{-1}$ are still in use that produce fine spectra. Despite representing only a few percent of the total absorption, EXAFS was also the first region of the XAS spectrum that found a theoretical interpretation resting on sound physical principles (Sayers et al. 1970; Stern 1974). Fitting methods with calculations based on Fourier analysis now provide quantitative data with a high degree of reliability (Sayers et al. 1971; Teo et al. 1977; Teo and Lee 1979). For a full coverage of the EXAFS method the reader is referred to classical works such as those by Lee et al. (1981), Hayes and Boyces (1982), Stern and Heald (1983), and Teo (1986), and to the recent review by Rehr and Albers (2000).

EXAFS structures occur in the form of wide, low-frequency oscillations that in most systems start at energies ca. 50~100 eV higher than the absorption threshold and progressively damp out to within 13~15 $Å^{-1}$ [k ($Å^{-1}$)= $\sqrt{2}m/(h/2\pi)^2$ (E - E_F)] or even more, depending on the edge of the measured atom and on the system (Borowski et al. 1999). These oscillations arise from back-scattering of photoelectrons of high kinetic energy involved in a single-scattering (SS) process with the nearest neighbors, during which the outgoing and back-scattered photoelectron waves undergo constructive and destructive interference. In the multiple-scattering formalism, EXAFS signals correspond to the single scattering paths of the photoelectron involved in the absorption process. EXAFS spectra can be analyzed to extract information about the distance from the absorber and its neighbors, in some cases extending to several shells as far away as ca. 0.6~0.7 nm (or even more in the case of super-focussing, when the arrangement of neighboring atoms in the structure is collinear: cf. Kuzmin and Parent 1994; Kuzmin et al. 1995) as well as about the number and type of the back-scatterers. The frequencies of the back-scattering photoelectron waves are roughly inversely proportional to the distance between the absorber and its neighboring atom shells. However, frequency and distance are not exactly proportional because the photoelectron undergoes a phase shift, as a result of the interaction of the outgoing and back-scattered waves with the potentials of the absorbing and back-scattering atoms. Such a phase shift is typically ca. 0.02-0.05 nm and is characteristic of a particular absorber to back-scatterer atom pair. The amplitude of the scattered wave reflects primarily the number and type of atoms located around the absorber, but it is reduced by the interference of several effects. Nevertheless, when all these limitations are well considered, the EXAFS function can be adequately modeled, in the single-scattering, spherical wave approximations, as being the sum of the scattering contributions from each shell of neighboring atoms up to a distance that may reach as much as ~0.5 to ~0.6 nm depending on the investigated system, this distance being determined by the inelastic losses undergone by the photoelectron along its mean-free path.

EXAFS provides information on the local structure around the absorber on an almost instantaneous time scale (10^{-16} s), so it is a most efficient method to detect time-dependent reactions or atom re-orderings for the investigated compound. However, the resolution of EXAFS for interatomic distances is bound to be large (±0.002 nm at best) because static and vibrational atom disorder in most solids is large. Furthermore, Holmes et al. (1988) showed that errors increase with the order of the investigated shell: they may be as low as ±0.001 nm for the first-shell distances, and up to ±0.005 nm for the fourth-shell ones. The determined coordination numbers are also affected by high errors, such as ~10% (i.e., ±0.2 atoms) for the nearest-neighbor shell, increasing to ~20% (i.e., ±0.5 atoms) for the second shell. For higher order shells, the error may be so large (ca. 50%) as to practically make the determination irrelevant. Normally, the coordination numbers determined by fitting EXAFS spectra are lower than the expected theoretical ones. Results become worse and worse as the coordination number increases, and may be very difficult to evaluate even when using complex analytical methods (Díaz-Moreno et al. 2000). Indetermination in the coordination numbers is also partially due to the presence of multi-electron processes superimposed on the EXAFS oscillations (Deutsch and Hart 1984; Filipponi et al. 1987; Chaboy et al. 1994).

In the analysis of EXAFS spectra, neglecting multi-electron excitations, all these effects are accounted for by the Debye-Weller factor, which measures the mean square deviation of the absorber to scatterer interatomic distance from its average length. In order to minimize these effects, EXAFS spectra are increasingly often recorded at low temperature, where the signal to noise ratio is higher than at ambient temperature, and the scanned reciprocal space longer. Yet, there are satisfactory EXAFS determination carried out at extremely high temperatures, and many limitations of the EXAFS technique in determining coordination numbers can be overcome using the additional information contained in the XANES region.

XANES

The XANES spectrum is certainly the most conspicuous and interesting part of the total absorption spectrum and, with the availability of third generation synchrotron radiation sources having brightness in the range 10^{15}~10^{21} photons·s^{-1}·mm^{-2}·mrad^{-2} (0.1% bandwidth)$^{-1}$, it can be recorded even for atoms highly diluted in the investigated material (trace elements: down to 50 ppm). Qualitative XANES analysis is now well established, and there is consensus that XANES spectra contain information on the oxidation state of the investigated atom, on its coordination in the structure, and on the form and orientation of the first-coordination polyhedron around it. However, XANES spectra for a long time were impossible to interpret quantitatively, and even now their full understanding is hampered by the complexity of the crystal structure of most minerals. However, XANES examination allows extraction of reliable information on the electronic and structural properties of the system under investigation. In fact, while in a crystalline material, that can be oriented in the scattering geometry, the pair distribution function may be sufficient to determine the complete crystal structure, in disordered materials (e.g., glasses) all directional information is lost. In other words, the radius of the first coordination sphere is not simply correlated with bond angles that involve at least the three-atom correlation functions. Thus, methods such X-ray diffraction (or neutron scattering, EXAFS, and others that do not provide more than the pair distribution function) make many subtle correlations of non-crystalline systems inaccessible. By contrast, XANES contain a structural information that is not confined to a pair correlation function between different atoms only, but it also explains atomic correlation functions at high order (Benfatto et al. 1986; Filipponi et al. 1990).

The generally strong scattering power of the atoms of the medium for low kinetic

energy photoelectrons favors multiple scattering (MS) processes. At higher energies such as those at which the atomic scattering power becomes small, a single scattering (SS) regime occurs. Consequently, by decreasing the photoelectron kinetic energy, a gradual transformation from the EXAFS regime to the XANES regime takes place. Therefore, the EXAFS part of the XAS spectrum probes the first-order or pair correlation function of the atomic distribution near the absorbing atom, while the XANES part probes the triplet and the higher orders of the atomic distribution function. Indeed, the growth of XANES was stimulated by interest in the determination of higher order correlation functions of local atomic distributions in complex systems and multiple-scattering theories have been used in recent years to solve the XANES spectra of crystals, amorphous solids, surfaces, biological molecules, liquids, catalysts and chemical compounds.

The first successful attempt at extracting this kind of information for metal atoms in both tetrahedral and octahedral coordinations was carried out on liquid systems (Garcia et al. 1986), and only recently have similar studies on solid systems become satisfactory (Wu et al. 1996; Mottana et al. 1997, 1999). However, XANES spectra are still difficult to fully interpret quantitatively, because experimental data sometimes exhibit such a richness in structures as to make it difficult to unravel them one by one, while theory has to face the significant problem of finding out a good potential that enables describing large atom clusters. Essentially: the period of "fingerprinting" use of XANES is over, and although significant theoretical work is in progress, the time of its full appreciation has not yet come, except for a few, fairly simple systems.

A XANES spectrum consists of a sequence of features (i.e., peaks) that are characterized for their relative intensity (generally given as arbitrary units) and energy position (eV). Indeed, although the general characteristics of the XANES spectra are mainly determined by the atomic distribution of the atoms neighboring the absorber (local site symmetry), while being almost independent of crystalline order, the observed features are actually system-dependent, particularly for their intensity. Consequently, XANES spectra are usually divided in three regions (Natoli and Benfatto 1986; Fig. 1):

(a) the edge region, or low-energy XANES region, from the absorption threshold (i.e., the energy of the first allowed transition, that represents the lowest energy state reached by the core excitations) up to ca. 10 eV above;

(b) the full-multiple-scattering (FMS) region, up to ca. 20-30 eV above the absorption threshold;

(c) the intermediate-multiple-scattering (IMS) region, from ca. 20-30 eV above threshold upwards to ca. 50-100 eV.

The edge region contains a few weak features caused by electronic transitions to empty bound states; the FMS region contains an infinite number of multiple-scattering contributions; and, finally, the IMS region contains a small number (e.g., $n < 4$) of multiple-scattering contributions that are limited only by the core-hole lifetime process and by the inelastic photoelectron-valence electron scattering, mainly related to the overall structural properties of the material. This last region is bound with and actually merges into

(d) the single-scattering (SS) region, which is the EXAFS region mentioned above.

The distribution of peaks and the ensuing separation of them in the three region is never straightforward, and in some systems they even overlap to a certain extent. However, if this theoretical description of XANES spectra is adopted (Natoli 1983; Natoli and Benfatto 1986; see Benfatto et al. 2001), then the two alternative theories of single- and multiple-scattering (Sayers et al. 1970 and Lee and Pendry 1975, respectively) can be unified and the treatment of the entire XAS spectrum traced back to a unique, complete, and physically coherent theory.

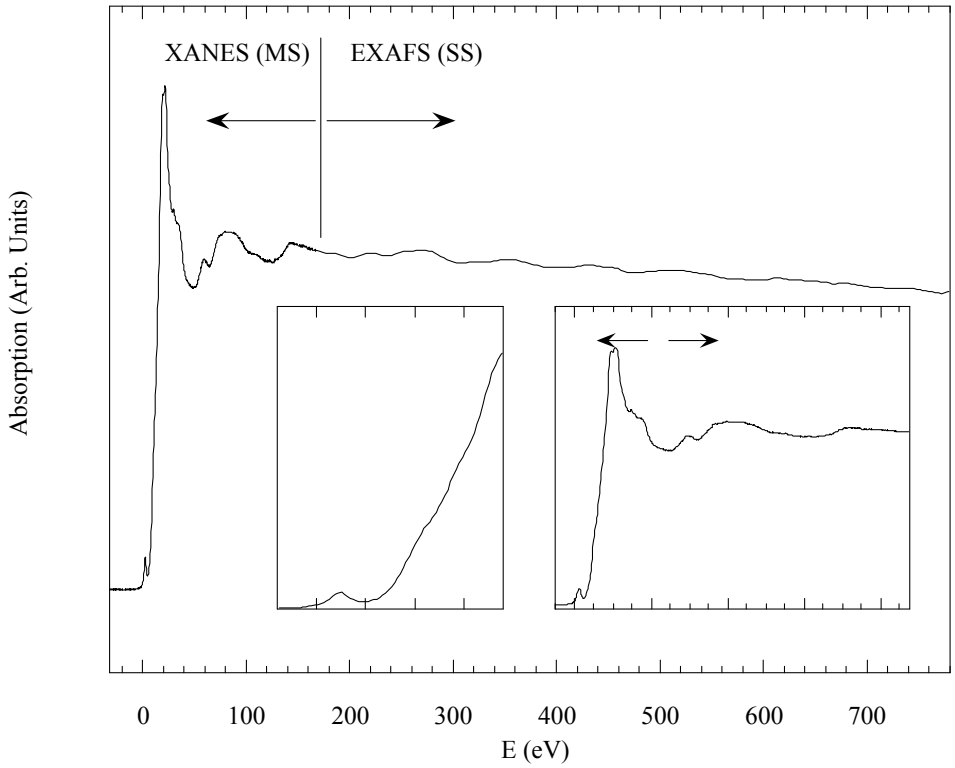

Figure 1. The full XAS spectrum of a high-Z atom showing (insets) the different energy regions discussed in the text: pre-edge (left) and edge (right) region. Traditionally, XANES is the region of the spectrum where the photoelectron undergoes multiple scattering, and EXAFS that of the single-scattering regime.

The ***edge region*** contains a few, normally weak features caused by electronic transitions to empty excitonic states that are controlled primarily by the selection rules for mainly dipolar (less quadrupolar) electronic transitions. These transitions can be explained by the molecular-orbital theory (Obashi 1978), which has been applied for many years to the interpretation of edge spectra. At the beginning, the quantum mechanical selection rules that control the transition probabilities in the edge region were considered to be the same as those for optical spectra (Brown et al. 1988), for which a theoretical framework was already known. Indeed, although Shulman et al. (1976) were the first to recognize that pre-edge features can arise from $1s \leftrightarrow 3d$ transitions (based upon the observation that Zn^{2+}, with a $3d^{10}$ configuration, has no pre-edge features), their entire assignment relied upon calculations, in the framework of the ligand-field theory, of the atomic or molecular final states of an atomic cluster that considered only the first shell. This theory proved to be inadequate. However, their method allows interpretation of the features occurring in the energy range 5 to 10 eV around the threshold only (pre-edge (PE) region). The first study that reached agreement between theory and experiment in the XANES study of solids, over a wide energy range that encompassed all the XANES region up to 50 eV above threshold, was by Bianconi et al. (1982). In that investigation, the experimental features in the XAS spectra of solids were associated to shape resonances, in which electrons are trapped in a molecular group, of the same type as those discussed by Dehmer and Dill (1976) for diatomic molecules.

The features just above the absorption threshold (called PE features) arise from different mechanisms: (1) the quadrupole mechanism (Balzarotti et al. 1980; Dräger et al. 1988); (2) the mixture of the transition metal 4*p*-states with the 3*d* ones owing to the non-

centrosymmetric symmetry of the coordination polyhedron around the absorbing atom ($p \leftrightarrow d$ mixture; Ravel et al. 1993), and (3) the dipole-allowed transitions of the transition metal 1*s* electrons to the unoccupied 3*d* states of the neighboring transition metal atoms (band effect: Bianconi et al. 1985; Uozumi et al. 1992; Vedrinskii et al. 1997). Several additional factors contribute to intensity and energy of features in the pre-edge region, including spin state, oxidation state, and site geometry.

The *intensity* of peaks is related to transition probabilities. The 1*s* $\leftrightarrow$ n*d* transitions in the pre-edge region are formally dipole-forbidden, but they have non-zero probabilities due to electric quadrupole transitions (Cabaret et al. 1999; Joly et al. 1999). This quadrupolar coupling is extremely weak (Hahn et al. 1982), about two orders of magnitude smaller than electric dipole coupling (Bair et al. 1980; Brouder 1990); however, in the cases where the cation occupies a non-centrosymmetric site, most of the intensity of the pre-edge features results from hybridization between the 3*d* and 4*p* states. In iron-bearing compounds, where the electric-dipole mechanism is fundamentally intense, a very small amount of 4 $p \leftrightarrow$ 3*d* mixing can have a dramatic effect on the intensity of the pre-edge feature (Roe et al. 1984; Randall et al. 1995; Westre et al. 1997). Consequently: (1) the greater the amount of 4*p* mixing into the 3*d* orbitals, the greater the intensity of the resultant pre-edge features; (2) the relatively symmetrical octahedral sites display little electric dipole coupling, but as site asymmetry increases, so does the 4*p* mixing into 3*d* orbitals. In micas, the tetrahedral sites have point symmetries of T_d, so they are more distorted than the octahedral sites for which point symmetries may be C_1, C_2, or C_{2h}. Accordingly, for a transition element occurring in both the tetrahedral and octahedral sites, the pre-edge tetrahedral peak will be far more intense. This effect is illustrated in Figure 2 for two micas that contain Fe^{3+} in different types of coordination (cf. Dyar et al. 2001).

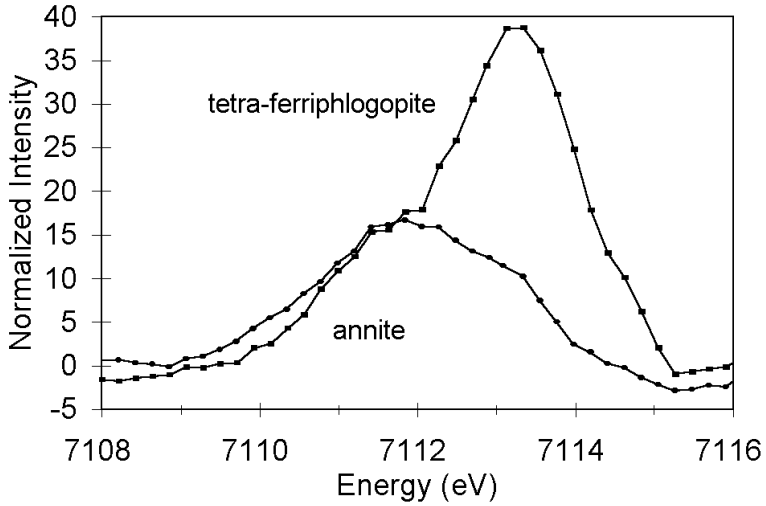

Figure 2. Effect of coordination on pre-edge peak intensity: the lower intensity spectrum is taken from a Pikes Peak annite, which has been shown to contain only octahedral Fe^{3+} and Fe^{2+}; the higher intensity spectrum is from a synthetic tetra-ferriphlogopite (after Dyar et al. 2001). Note that peak positions and intensities vary independently, and as a function of both coordination and oxidation state.

Brown et al. (1988) quantified the increase in pre-edge intensity to be from 0.7~2.0% of the main edge for $^{[6]}Fe^{2+}$, to 5~7% of the main edge for $^{[4]}Fe^{2+}$, and up to 15% of the main edge for $^{[4]}Fe^{3+}$. Galoisy et al. (2001) further noted that pre-edge intensity varies

inversely with coordination number for non-centrosymmetric environments, such that $I_{oct} < I_{5\text{-fold}} < I_{tet}$. Finally, the transition probability (and thus the relative intensity of the peak) is increased if the number of empty states in the *d* orbitals is large. For example: the pre-edge spectrum of a mineral containing vanadium, an atom which may occur in four valence states (V^{2+}, V^{3+}, V^{4+}, and V^{5+}, having configurations of $3d^4$, $3d^3$, $3d^2$, and $3d^1$, respectively), would be most intense for the V^{5+} (Delaney et al. 2000; cp. Wong et al. 1984; and also Cressey et al. 1993, and Schofield et al. 1995, for *L*-edge spectra).

The *energy position* of the peaks in the pre-edge region is also important, because it has a first-order relationship to oxidation state. Shulman et al. (1976) showed that pre-edge transitions differ from their analogous optical transitions because the number of transitions present (i.e., the strong field many-electron states) must be modeled for the $d^{(n+1)}$ excited state. This assumes that the dominant effect of the 1*s* core-hole is an increase in potential because it is spherically symmetrical (Westre et al. 1997). This 1*s* hole is so close to the nucleus that the outer orbitals see a configuration equivalent to that of the next highest ion in the periodic chart, with a fully occupied 1*s* shell. So, the final state of the ion, rather than having an atomic number Z with a 1*s* hole, is instead best approximated by that of a different nucleus with atomic number Z+1 (Shulman et al. 1976; Lee and Beni 1977): XANES spectra will show the energy levels predicted by the optical spectra for these Z+1 states. For example, the best analogs for Fe XANES spectra are Co optical spectra (of which, unfortunately, there are relatively few). However, for minerals, studies of this type on the pre-edge region are rare. Thus, it is necessary to fall back upon simple models based on fundamental principles. Tanabe-Sugano diagrams have been calculated for most simple coordination polyhedra, and from these the identity, if not the precise energy, of the peaks in any given pre-edge can sometimes be approximated.

Only recently have the energy separations of the pre-edge features of elements in different oxidation states and coordinations precisely been measured: e.g., in a series of minerals excluding the micas Petit et al. (2001) determined the energy separation between the average pre-edge centroid positions for Fe^{2+} and Fe^{3+} to be 1.4 ± 0.1 eV. Additionally, the pre-edge transitions for Fe in different coordination polyhedra relevant to micas can be summarized as follows (Calas and Petiau 1983; Galoisy et al. 2001): (1) $^{[6]}Fe^{2+}$ pre-edges should be composed of (at least) three peaks corresponding, from lowest to highest energies, to the $T_{1g}(^4F)$, $T_{2g}(^4F)$, and T_{1g} (^4P) states respectively; a fourth predicted transition, A_{2g}, is not visible because it is a two-electron transition with low probability. For Fe^{3+} in either tetrahedral or octahedral coordination, two electronic transitions are expected: (2) for $^{[6]}Fe^{3+}$, the $^5T_{2g}(^5D)$ state is lower in energy than the $^5E_g(^5D)$ state by approximately 1.1~1.5 eV (Westre et al. 1997); (3) for $^{[4]}Fe^{3+}$, the states reverse in energy, as expected, on going from the octahedral to the tetrahedral coordination, with a smaller separation of about 0.6 eV (Westre et al. 1997), as predicted by crystal field theory.

Given that the current peak width with existing technology is roughly 0.9 eV, the $^{[6]}Fe^{3+}$ transitions can barely be resolved, and the $^{[4]}Fe^{3+}$ site shows only a single intense pre-edge. Furthermore, distortions from ideal octahedral symmetries to tetrahedral and square pyramidal geometries (as are found in most mineral spectra) allow for $3d \leftrightarrow 4p$ mixing, and affect both the intensity and energy distribution in the pre-edge region. So, while these simple models (three component peaks in pre-edge spectra of $^{[6]}Fe^{2+}$, two for $^{[6]}Fe^{3+}$, and one for $^{[4]}Fe^{3+}$) represent the best approximations for currently available data, we await better technology for higher resolution to improve our understanding of the complexity of transitions represented in the pre-edge region of micas, the more so as very satisfactory pre-edge calculations have been proven to be feasible in other systems (Ruiz-

López and Muñoz-Páez 1991) even in the polarized setting, which best accounts for the layered structure of the micas (Joly et al. 1999).

The ***full multiple-scattering (FMS) region*** of a XANES spectrum is dominated by multiple-scattering resonances of photoelectrons ejected at low kinetic energy, even when the binding energy is great. In particular, this region contains several intense resonances (including the white-line, i.e., the most intense resonance) that arise from superposition of contributions from the multiple-scattering interactions undergone by the photoelectron along its pathways, as well as from the atom electronic properties. Thus, most information contained in the FMS region relates to long- as well as short-range order, but all contributions are interwoven in such a way as to make interpretation in terms of multiple-scattering rather difficult. Only lately has suitable de-convolution software been developed (Benfatto et al. 2001) that is based on sound physical principles rather than being a mere mathematical peak fitting. Therefore, information on the electronic properties of the system can now be obtained.

The FMS region of XANES spectra may provide information about bond length. Indeed, the continuum part of the spectrum, where multiple-scattering features of the photoelectrons can be easily resolved, is sensitive to both coordination geometry and interatomic distances. The effect of the interatomic distance d has been shown to shift the multiple-scattering resonances, first in diatomic molecules with a given geometry (Dell'Ariccia et al. 1984; Bianconi et al. 1985), following the relationship $k_r\, d = const$, where k_r is the wave vector of the photoelectron at resonance; this relationship is valid only for small variations of d (< ~10%).

In solid compounds, the extraction of this kind of information is essentially based on the relationship known as Natoli's rule (1983, 1985):

$$E_r - E_b = \text{const} / d_{(A\text{-}L)}^2$$

where E_r and E_b are the energies of the resonance feature and of the electron bound state, respectively, and $d_{(A\text{-}L)}$ is the distance from the absorber to its ligand. This formula does not need any determination of average interstitial potential, and is certainly true for the bound states at the K edges of transition metals (e.g., 1s to 4p transition). One of the major fields of application for such a formula is related to disordered or non-crystalline materials. However, it is seldom used for crystalline substances and, in particular, it has never been applied to any mica.

The ***intermediate multiple-scattering (IMS) region*** is a region that shares the multiple-scattering behavior of XANES and the single-scattering behavior of EXAFS. It usually consist of few, fairly weak and broad features (however sharper and stronger than the SS oscillations that follow) that mostly arise from interactions of the photo-electron with atoms in distant shells, at a high order (e.g., 4th or even 6th shell: Cabaret et al. 1996; Wu et al. 1996), or with preferential paths inside the first shell. This implies that the IMS region is strongly affected by the medium- to long-range orders of the studied structure, so that the similarity of IMS regions often represents a substantial proof of overall structure identity among the members of a complex solid solution series undergoing chemically-driven structural ordering (e.g., omphacite pyroxenes: Mottana et al. 1997, 1999).

Multiple scattering theory. At the end of this general overview of the practice of XAS spectroscopy, a short overview of the underlying theory is advisable that will clarify some statements otherwise acritically given. The short presentation that follows is based on the multiple-scattering theory as developed over the years by C.R. Natoli and coworkers (Natoli 1983; Natoli and Benfatto 1986; Natoli et al. 1980, 1990; Tyson et al.

1992). Natoli's approach unifies various schemes of interpretation, including, pioneering schemes such as the "one-electron single-scattering" approach to EXAFS by Sayers et al. (1970, 1971; see also Stern 1974) and Lee and Pendry (1975; see also Pendry 1983), the "one-electron multiple-scattering" approach by Dehmer and Dill (1976), and finally those based on band calculations by Müller et al. (1982). In this way, he was able to reach a complete physical theory.

The absorption cross section for X-rays may be written in the dipole approximation as

$$\sigma(E) = 4\,\pi^2\,\alpha\,E\,\Sigma_f\,|M_{if}|^2\,\delta(E_i - E_f + E)$$

$$M_{if} = \int \Psi_f^*(r_1, r_2, \ldots, r_n)\,\Sigma_n\,(r_n.\boldsymbol{\varepsilon})\,\Psi_i(r_1, r_2, \ldots, r_n)\,dr$$

where $\boldsymbol{\varepsilon}$ is the polarization vector of the electric field and the r_n is the vector describing the position of the n-th electron. The mathematical problem to solve is the calculation of the cross-section and in particular the description of the final state of the system, in accordance with the proper normalization and boundary conditions. Actually, three methods have been used to reproduce the experimental absorption cross sections σ(E) in both XANES and EXAFS regions:

(a) an approach based on the band calculations where the final states of the systems are Block states and the sum is performed on a Brillouin zone (Müller et al. 1982; Müller and Wilkins 1984);

(b) a method based on the wave function approach of the system with appropriate boundary conditions (Natoli and Benfatto 1986);

(c) a Green's function approach, i.e., a calculation of the scattering solution of the Schrödinger equation of the excited photoelectron, and of the proper boundary conditions (Durham et al. 1982; Benfatto et al. 1986).

In the next paragraphs, we will briefly outline the multiple-scattering theory within the framework of a single-particle approximation. The multiple-scattering method has been developed in nuclear physics to calculate nuclear scattering cross-sections and in solid state physics to compute the electronic structure of solids. Indeed, this method represents an extension of the bound-state molecular scattering method used by Johnson (1966, 1973) to determine the one-electron wave function for continuum states. In this scheme, the total potential is represented by a cluster with non-overlapping spherical potential centered on the atomic sites (typically three or four shells around the absorbing atom). The Coulomb and exchange parts of the input potential are calculated on the basis of a total charge density obtained by superimposing the atomic charge densities, calculated from Clementi and Roetti's (1974) tables of the individual atoms constituting the cluster. For the exchange potential it is possible to use either the usual energy-independent Slater (1979) X-α approximation or the energy-dependent Hedin-Lundqvist (1971) potential in order to incorporate the energy-dependent exchange and screening effects as well as extrinsic losses (local plasmon excitations).

To clarify the physical implication of the cross-section of the photoabsorption process discussed in the previous sections, it is better to use the Green's function approach with a generalized optical theorem (Natoli et al. 1986), and to write the following expression for the cross section

$$\sigma(E;\boldsymbol{\varepsilon}) = -k/\pi\;4\pi^2\,E\,\alpha\,\Sigma_{LL'}\,m_L(\boldsymbol{\varepsilon})\;\mathbf{Im}\{(\mathbf{I} + \mathbf{T}_a\mathbf{H}) - 1\mathbf{T}_a\}_{LL'}\,m_{L'}(\boldsymbol{\varepsilon})$$

where $m_L(\boldsymbol{\varepsilon})$ is the matrix element, which selects the final L by the dipole selection rule.

In this expression, $\mathbf{T}_a = \delta_{ij}\,\delta_{LL'}\,t_l^i$, where t_l^i is the atomic t-matrix element of the atom

at site i, describing its scattering power for a *l* spherical wave incident on it, while $\mathbf{H} = H^{ij}_{LL}(1 - \delta_{ij})$ is the free amplitude propagator of the photoelectron in the spherical wave state from site i with angular momentum L to site j with angular momentum L' and $\mathbb{I}$ is the unit matrix. Looking with care at the last equation, it is clear that all the geometrical information about the medium around the photoabsorber is contained in the inverse matrix $(\mathbf{I} + \mathbf{T}_a\mathbf{H})^{-1}$. When the modulus of the maximum eigenvalue, $\rho(\mathbf{T}_a\mathbf{H})$, of the matrix $\mathbf{T}_a\mathbf{H}$ is less than one, it is possible to expand the inverse in series (Natoli and Benfatto 1986) that are absolutely convergent relative to some matrix norm, so that

$$\sigma(E;\boldsymbol{\varepsilon}) = \Sigma_{n>0}\, \sigma_n(E;\boldsymbol{\varepsilon})$$

where

$$\sigma_n(E;\boldsymbol{\varepsilon}) = -4\pi\, E\, \alpha\, \kappa\, \Sigma_{LL'}\, m_L(\boldsymbol{\varepsilon})\, \mathbf{Im}\{(-1)^n\, (\mathbf{T}_a\mathbf{H})^n\, \mathbf{T}_a\}_{LL'}\, m_{L'}(\boldsymbol{\varepsilon}).$$

In this expression, the term n = 0 represents the smoothly varying "atomic" cross section while the generic n term is the contribution to the photoabsorption cross section coming from processes in which the photoelectron has been scattered (n - 1) times by the surrounding atoms before returning to the photoabsorbing site. The unpolarized absorption coefficient, which is proportional to the total cross section, is given by (Benfatto et al. 1986):

$$\alpha_F \approx h\nu\, \{(l + 1)\, M_{l,l+1}\, \chi_{l+1} + l\, M_{l,l-1}\chi_{l-1}\}$$

where *l* is the orbital angular momentum of the core initial state (*l* = 0 for a *K* level), $M_{l,l\pm1}$ is the atomic dipole transition matrix element for the photoabsorbing atom, and

$$\chi_l = \{(2l + 1)\, \sin^2\delta_l^0\}^{-1}\, \Sigma_m\, \mathbf{Im}\, \{(\mathbf{I} + \mathbf{T}_a\mathbf{H})^{-1}\mathbf{T}_a\}_{lm,lm}$$

is the quantity that contains the structural geometrical information. Here, δ_l^0 is the phase shift of the absorbing atom. The total absorption coefficient can be expanded as a series

$$\alpha_F = \alpha_0\, (1 + \Sigma_{n>2}\, \chi_n)$$

where the first element α_0 is the atomic absorption coefficient and the second term α_1 is always zero because $H_{lm,lm} = 0$. For the *K* edge, in the plane-wave approximation, the expression for n = 2 is the usual backscattering amplitude, i.e., the EXAFS signal times the atomic part. Actually, the first multiple-scattering contribution is the α_3 term, which can be written (Benfatto et al. 1989) as

$$\alpha_3 = \alpha_0\, \Sigma_{i\neq j}\mathbf{Im}\, \{\, P_1(\cos\phi)\, f_i(\omega)\, f_j(\theta)\, \exp(2i(\delta_l^0 + kR_{tot}))/kr_ir_{ij}r_j\, \}$$

where r_{ij} is the distance between atoms i and j, $f_i(\omega)$ and $f_j(\theta)$ are the relative scattering amplitudes, which now depend on the angles in the triangle that joins the absorbing atom to the neighboring atoms located at sites $\mathbf{r}_i$ and $\mathbf{r}_j$, and $R_{tot} = r_i + r_{ij} + r_j$. In this expression, $\cos\phi = -\,\mathbf{r}_i\cdot\mathbf{r}_j$, $\cos\omega = -\mathbf{r}_i\cdot\mathbf{r}_{ij}$ and $\cos\theta = \mathbf{r}_i\cdot\mathbf{r}_{ij}$. As a consequence, the n = 3 term and all terms with n higher than 2 contain information about the higher order correlation function. It is possible to observe also that, in this framework, because of $P_1(\cos\phi) = \cos\phi$, there is a selection rule in the pathways. As an example, consider the α_3 term: in all the cases where r_i is perpendicular to r_j, the corresponding MS term does not contribute to the total cross section because $\cos\phi = 0$. Neglecting multi-electron contributions, this description makes clear the distinction between the FMS and IMS regions in a XANES spectrum, and assigns any differences to the local geometrical structure of the system.

In a practical way, in the analysis of XANES spectra of condensed systems the first step is to identify the size of the relevant cluster of atoms (Garcia et al. 1986; Benfatto et al. 1986), i.e., the cluster of atoms around the central absorbing atom. The size of this cluster may range from the smallest one, including only the nearest neighbors, to clusters including several surrounding shells. Neither translation symmetry nor site symmetry of such a cluster is required, and the finite size of the cluster is determined only by the mean free-path for elastic scattering of the photoelectron and by the core-hole life time. In the energy range 1~10 eV, where the mean free-path becomes longer than 0.1 nm, the size limitation due to the core-hole lifetime is the most important parameter. Actually, the contribution of further shells can be reduced or cancelled out by different degree of structural disorder.

Experimental spectra recording

Recent advances in X-ray spectroscopy of minerals are mainly related to the development of synchrotron radiation sources that overcame the limitations in energy range, intensity and stability of radiation that conventional X-ray tubes had. Currently, the availability of third generation electron storage rings and of special sources generated by insertion devices (wigglers and undulators) offers brilliant, tunable, and polarized sources in a wide range of energy, from IR to hard X-rays, and opens up new opportunities to all material sciences.

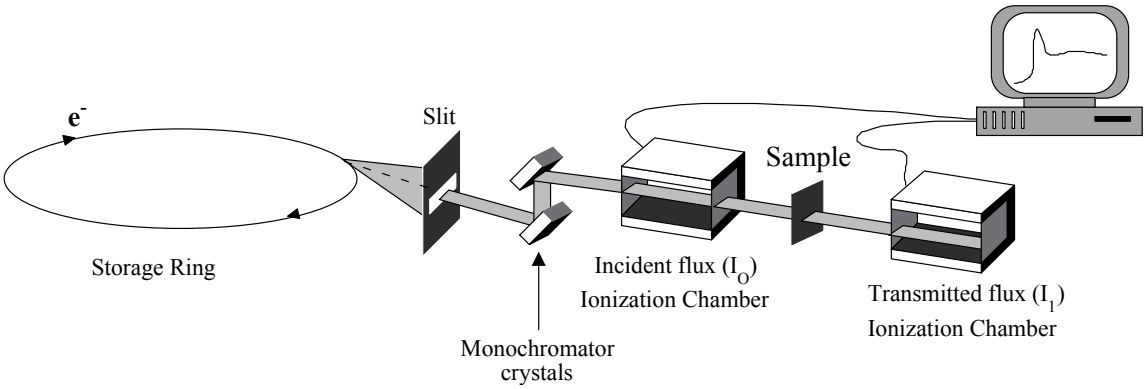

Figure 3. Schematic representation of a modern experimental setup for X-ray absorption spectroscopy in the transmission mode.

A schematic view of an experimental setup at one modern facility for X-ray absorption spectroscopy studies in the conventional transmission mode is shown in Figure 3. However, experimental setup and detection methods depend on several factors, the most important being the energy range of the X-rays to be used. In turn, this strictly depends upon the absorption edges to be analyzed. In the study of micas, it is opportune to investigate both low Z atoms (i.e., Na, Mg, Al, Si, K, etc.) and high Z atoms (e.g., Ti, V, Cr, Mn, Fe, etc). Such different energy ranges require different types of monochromators: (1) the soft X-ray energy range (<1 KeV) needs glancing incidence grating monochromators; (2) the X-ray energy range 1~3 KeV needs special crystals like YB_{66} (Wong et al. 1990, 1999), InSb, quartz or beryl; and (3) the hard X-ray energy range (>4 KeV) requires double reflection Si or Ge crystals, the reflecting crystal plane being properly chosen to the purpose of achieving best resolution and high intensity. Moreover, the soft X-ray range requires special beam lines and experimental chambers and, because of the strong absorption of the radiation at these wavelengths in air, high (HV) or ultra-high vacuum (UHV) conditions are compulsory. The strong photon absorption of gases prevents the use of photo-ionization chambers; thus, in HV or UHV

conditions, electron detection systems are usually employed. Metal grids can be used to monitor beam intensity, either by means of electron multipliers (channeltron) that collect all electrons extracted by the photon beam, or by direct measurement of the drained photo-electron current (Stöhr et al. 1980).

The *detection system* depends on the concentration of absorbing atoms in the material and photon energy. For bulk experiments using hard X-rays (i.e., with $h\nu >$ 4 KeV) on samples with concentrations above 10^{-3} (atomic ratio), standard X-ray transmission techniques are used. The incident and transmitted fluxes are typically measured by photo-ionization chambers. In the soft X-ray range (i.e., with $h\nu < 1000$ eV), absorption spectra may be efficiently measured by recording core-hole decay products. If we describe the inner-shell photo-ionization process as a two-step process, then in the first step the photon excites a core-hole electron pair, and in the second step the recombination process of the core-hole takes place. There are many channels suitable for core-hole recombination. These channels may produce the emission of photons, electrons, or ions, all of which are collected by special detectors. The recombination channel that is normally used to record bulk XAS spectra of dilute systems is the direct radiative core-hole decay that produces X-ray fluorescence lines. When fluorescence lines have high photon energies, this technique probes the bulk. In Figure 4 a beam line with an apparatus to record absorption spectra in the fluorescence mode is schematically represented.

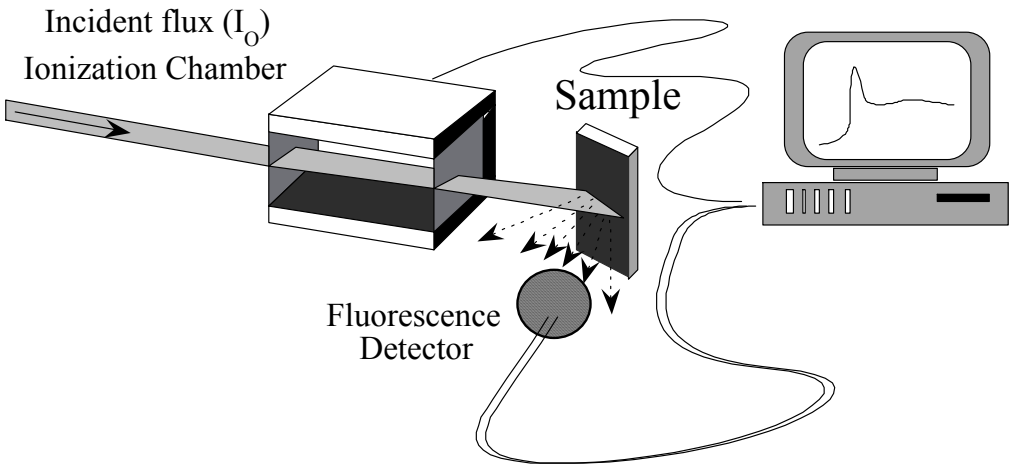

Figure 4. Schematic representation of an apparatus designed to record X-ray absorption spectra in the fluorescence mode.

In the soft X-ray range, the Auger recombination has a higher probability than the radiative recombination (Stöhr et al. 1984). Because the energy of the Auger electrons is characteristic of a particular atom, the selective photoabsorption cross-section of an atomic species (in particular those chemisorbed on a surface) can be measured by monitoring the intensity of its Auger electrons as a function of photon energy. An intense Auger line is selected by an electron analyzer operating in constant final state (CFS) mode with an energy window of a few eV. A standard experimental setup for this type of XAS measurement is shown in Figure 5 (modified after Stöhr et al. 1984). Note, however, that Auger electrons arise from the uppermost impinged layers of atoms; consequently, this type of measurement is essentially probing the surface of the sample, i.e., it competes with surface EXAFS (i.e., SEXAFS), rather than with bulk XAS. For

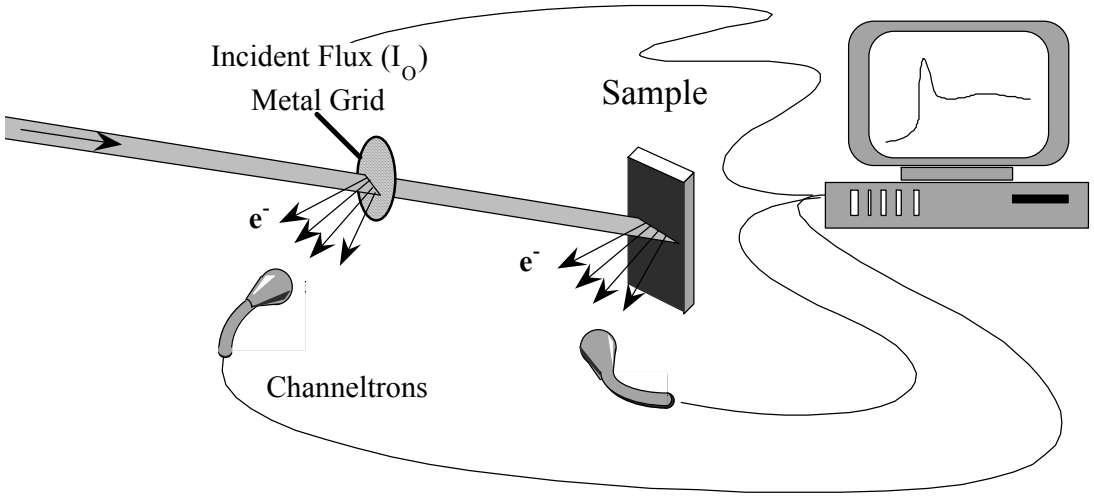

Figure 5. Schematic representation of a standard experimental setup for surface X-ray absorption measurements.

bulk measurements, the total electron yield (TEY), which has been found to be proportional to the absorption coefficient (Gudat and Kunz 1972), is used. This technique measures the integral yield over the entire energy range of the emitted electrons. The advantage of this method is that maximum counting rates are obtained, since all the emitted electrons over a large solid angle can be collected by applying a positive voltage to the detector. Another detection method used is the low-energy partial electron yield (PEY), where only the secondary electrons within a kinetic energy window around the maximum in the inelastic part of the electron energy distribution curve (EDC) are collected. Because of the long escape depth for low-energy electrons, the bulk absorption recording with this method makes use of an electron analyzer.

High *resolution*, on the order of 0.15-0.2 eV (i.e., a resolving power in the range 10^4), is experimentally demanding in XANES spectroscopy because important physical information can be extracted from small variations in the intensity and/or energy shift of an absorption peak. For this reason, careful preparation of homogeneous pinhole-free samples and suppression of high harmonics in the incident photon beam are required. Using crystal monochromators, the energy band width ΔE of the photon beam monochromatized by Bragg diffraction is determined by the angular divergence $\Delta\Theta$ and by the crystal rocking curve. In synchrotron radiation beam lines, the angular divergence depends upon the intrinsic vertical spread of the radiation, which is determined by both the energy of the electron beam circulating in the storage ring and the source size, i.e., the diameter of the electron beam and its divergence at the emission point as determined by the electron optics. Resolution can be improved by changing either the crystal or the reflection plane. In a double-crystal monochromator, two parallel reflections produce a monochromatised photon beam parallel to the incident one. These two reflections reduce the tails of the rocking curve, and consequently increase the resolution, but they leave the higher-order harmonic reflection content like that of a single reflection (Greaves et al. 1983). Less common are other types of high-resolution crystal monochromators with special geometries that make use of antiparallel reflections. Finally, high-resolution XANES spectra may be measured using higher-order reflections. Harmonic rejection may be achieved in devices with two crystals by detuning one crystal with respect to the other. In fact, when the two crystals are misaligned, the intensity of the harmonics drops off much more rapidly than the intensity of the fundamental, because bandwidth $\omega_n(\lambda)$ is

much narrower for n > 1 harmonics than for the fundamental one. The higher-order harmonic content in the synchrotron radiation beam is due to the intense continuum of the primary beam extending towards high energies, and it represents a significant contribution in all the high-energy third-generation synchrotron sources. Actually, rejection of higher-order harmonics may be obtained using either mirrors behaving as low-band pass filters, and/or by detuning crystals, or even by means of undulator sources.

Optimization of spectra

Orientation effect. Most experimental XANES spectra on micas were measured on powders, obtained by grinding hand-picked grains that had been gently settled on a flat sample-holder after dispersion in a liquid. The resulting mounts were considered to be randomly oriented, regardless of their grain-size homogeneity and distribution. However, experience gathered on other sheet-silicates (e.g., Manceau 1990; Manceau et al. 1988, 1990, 1998) has shown that, even in fine-grained powders, crystallite orientation strongly affects the shape of the final spectrum: primarily, it changes peak intensity, which is a significant component of the information and certainly reflects onto its quality (see above). If this is indeed the case, then among the mica XANES spectra performed so far (Table 2) only a few can be considered to be reliable. These include work by Osuka et al. (1988, 1990), Mottana et al. (1997) and Sakane et al. (1997), in which no special care was taken, but the investigated micas, being synthetic, were so homogeneously fine-grained (1 μm) as to certainly lie on the sample-holder with their **c** axis more or less orthogonal to its surface and with their **a** and **b** axes oriented at random on it.

A theoretical study of the orientation effect has been recently presented for self-supporting clay-mineral thin films by Manceau et al. (1998), who also propose a tridimensional system of coordinates to record spectra in a standard setting. Their method, slightly modified by Cibin et al. (2001), has been adopted by Mottana et al. (in preparation) for single crystal mica blades (Fig. 6). Another approach used by Dyar et al. (in prep.) uses mica single crystals mounted on fibers in goniometer heads, which are then fitted onto a spindle stage mounted with the plane of rotation perpendicular to the path of the beam.

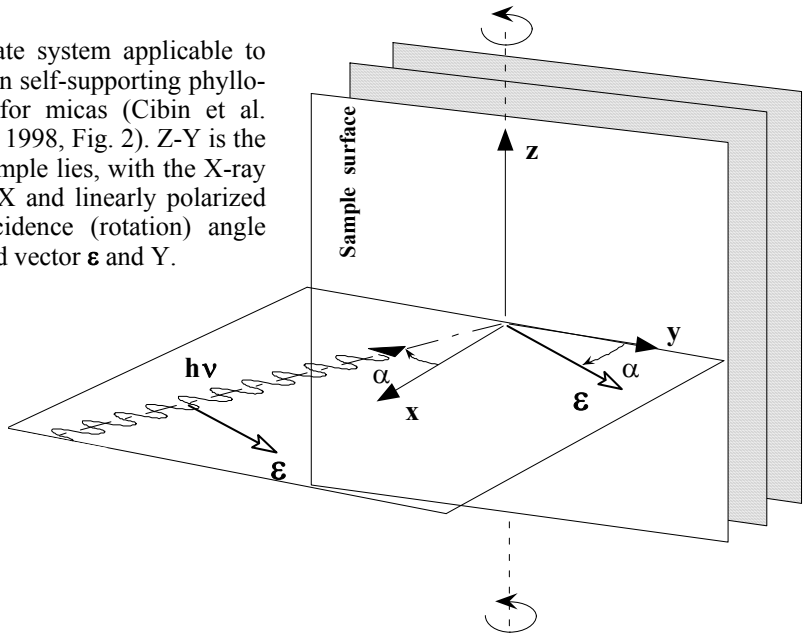

Figure 6. The coordinate system applicable to angular measurements on self-supporting phyllosilicate films as used for micas (Cibin et al. 2001; cf. Manceau et al. 1998, Fig. 2). Z-Y is the plane onto which the sample lies, with the X-ray beam impinging along X and linearly polarized on X-Y; α is the incidence (rotation) angle between the electric field vector **ε** and Y.

For a perfectly random distribution of very small crystals (powder) there would be no angular variation effect on the experimental XAS spectra; however, for a fully oriented crystal structure such as that of a mica blade lying flat on the sample-holder, the amplitude of the scattered photoelectron wave depends on the angle α between the

electric field vector **ε** of the impinging beam and the layers in the structure. This angle can be determined either by rotating the sample-holder on its vertical axis, or by preparing suitably oriented thin sections to be glued on the sample-holder in its routine setting orthogonal to the X-ray beam ($\alpha = 0°$).

Mottana et al. (in preparation) operated at SSRL at the 3-3 beamline (Hussain et al. 1982; Cerino et al. 1984), which is equipped with a double-crystal monochromator made

Table 2. Published XAS data on mica species materials.

SPECIES	ATOM	REFERENCE
DIOCTAHEDRAL		
celadonite	Fe	Drits et al. (1997)
illite (Ti)	Ti	Huggins & Huffman (1996)
illite	K	Huggins & Huffman (1996)
illite	Fe	Drits et al. (1997)
illite	I	Fuhrmann et al. (1998)
muscovite	V	Jagannatha Rao & Chetal (1982)
muscovite	Si	Brytov et al. (1979) Li et al. (1995a)
muscovite	K	Huggins & Huffman (1996)
muscovite	Fe	Jagannatha Rao & Chetal (1982) Jain et al. (1980)
muscovite	Cr	Brigatti et al. (2001) Calas et al. (1984) Jagannatha Rao & Chetal (1982)
muscovite	Al	Doyle et al. (1999) Mottana et al. (1997) Li et al. (1995b) Ildefonse et al. (1994) Brytov et al. (1979)
TRIOCTAHEDRAL		
bityite	Al	Mottana et al. (1997)
ephesite	Al	Mottana et al. (1997)
phlogopite	Cr	Kemner et al. (1997)
phlogopite	Fe	Jain et al. (1980)
phlogopite	Fe	Cruciani et al. (1995)
phlogopite	Si	Brytov et al. (1979)
phlogopite	Al	Brytov et al. (1979)
phlogopite (F)	Co	Osuka et al. (1988)
phlogopite (F)	Mn	Osuka et al. (1990)
phlogopite (F)	Al	Mottana et al. (1997)
polylithionite (F)	Al	Mottana et al. (1997)
preiswerkite	Al	Mottana et al. (1997)
tainiolite (Na)	Ba	Sakane et al. (1997)
tainiolite (Na)	Cs	Sakane et al. (1997)
tainiolite (Na)	Rb	Sakane et al. (1997)
tainiolite (Na)	Sr	Sakane et al. (1997)
tetra-ferriphlogopite	Fe	Cruciani et al. (1995)
tetra-ferriphlogopite	Fe	Dyar et al. (2001)
tetra-ferriphlogopite	Fe	Giuli et al. (2001)
zinnwaldite (Mg)	Al	Mottana et al. (1997)
SYNTHETIC(as yet unknown)		
tetrasilicic Na fluormica	Na	Soma et al. (1990)
tetrasilicic Na fluormica	Nd	Han et al. (2001)
SERIES NAMES		
biotite	Al	Li et al. (1995b)
biotite	Fe	Bajt et al. (1995) Heald et al. (1995) Manceau (1990) Manceau et al. (1990) Güttler et al. (1989) Manceau et al. (1988) Jain et al. (1980) Dyar et al. (2001)
biotite	I	Fuhrmann et al. (1998)
biotite	Si	Li et al. (1995a)
biotite	Ti	Waychunas (1987)
illite	Cs	Kemner et al. (1997)
illite	Fe	Drits et al. (1997)
illite	I	Fuhrmann et al. (1998)
illite	K	Spiro et al. (1984)

of efficient crystals such as YB_{66} (Wong et al. 1990 1999). They scanned single-crystal mica blades lying flat on the vertical sample-holder and optically-oriented in such a way as to have **a** ≅ **b** // Z. Here Z is an axis lying parallel to the mica surface (Fig. 6). The synchrotron beam first impinges the mica at right angle ($\alpha = 0°$); then the blade is rotated and α increased up to 60~80°, this being the maximum angle allowed by the mechanics of the sample compartment and the geometry of detection, which uses channeltrons. Therefore, the electric vector **ε** always lies on the horizontal plane, but it impinges two almost perpendicular sections of the mica structure so as to scan its atoms under different angles, with their atomic bonds and angles geometrically modified.

The orientation effects observed in this way are clearly visible in a natural muscovite compositionally close to the end member (Fig. 7). It is quite clear that orientation dramatically affects the intensity of all peaks, including the white-line, but also—although to a much lesser extent—the positions of some of them, by as much a 5 eV. A comparison between Figure 7 and the Al *K*-edge spectrum reported by Mottana et al. (1997; cf. Fig. 4) for synthetic muscovite, which is expected to be randomly oriented owing to its very fine-grained powdery nature, shows that best agreement is attained for a rotation angle α in between 45 and 70°.

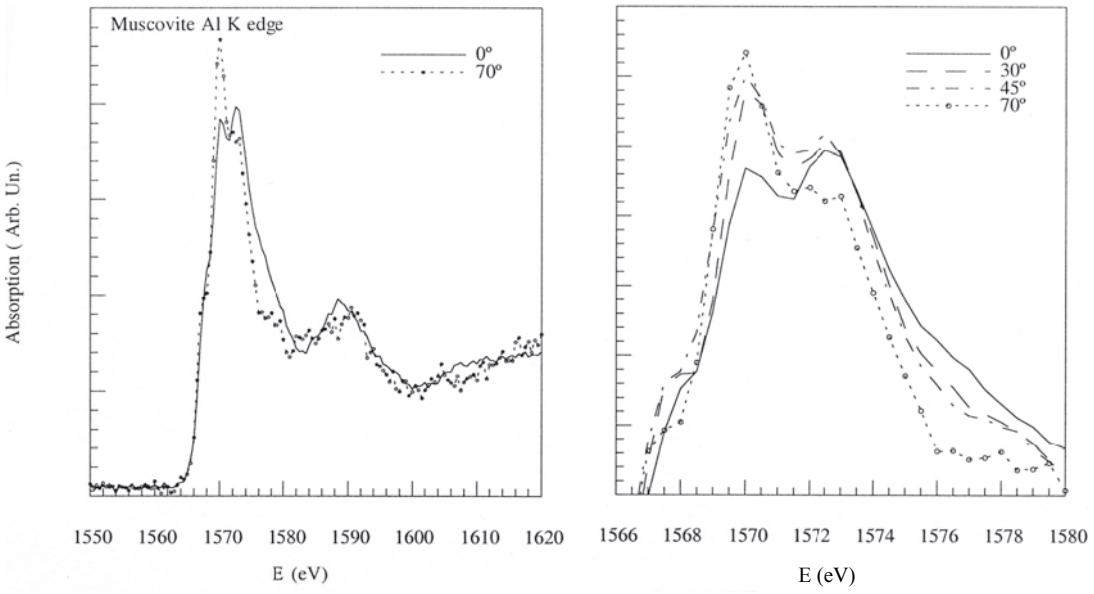

Figure 7. Changes in an Antarctica muscovite Al *K*-edge spectrum due to changing the orientation of the same crystal blade against the impinging, horizontally-polarized synchrotron radiation beam. In the right panel a magnified view of the white-line intensity as a function of the α rotation angle.

A similar comparison between the Fe *K*-edge spectra of a phlogopite single crystal rotated in the same way (Fig. 8) and the several Fe XANES spectra of phlogopites in the literature (Table 1) confirms that best agreement is obtained when the crystal is rotated at α ca. 45°. Indeed, later work (unpublished) showed that best agreement for the same sample, when scanned as both single crystal (at various angles) and as a settled homogeneous powder having a grain size of ca. 5 μm, is obtained when α is equal or very close to the "magic angle" value 54.7° (Pettifer et al. 1990).

Changes with orientation are also clearly evident in the XANES spectra of a number of di- and tri-octahedral micas and one brittle mica, respectively at the Mg (phlogopite: Fig. 9), Si (muscovite: Fig. 10, and tetra-ferriphlogopite: Fig. 11), K (muscovite: Fig. 12), and Fe (clintonite: Fig. 13, and tetra-ferriphlogopite: Fig. 14) *K* edges. Such changes

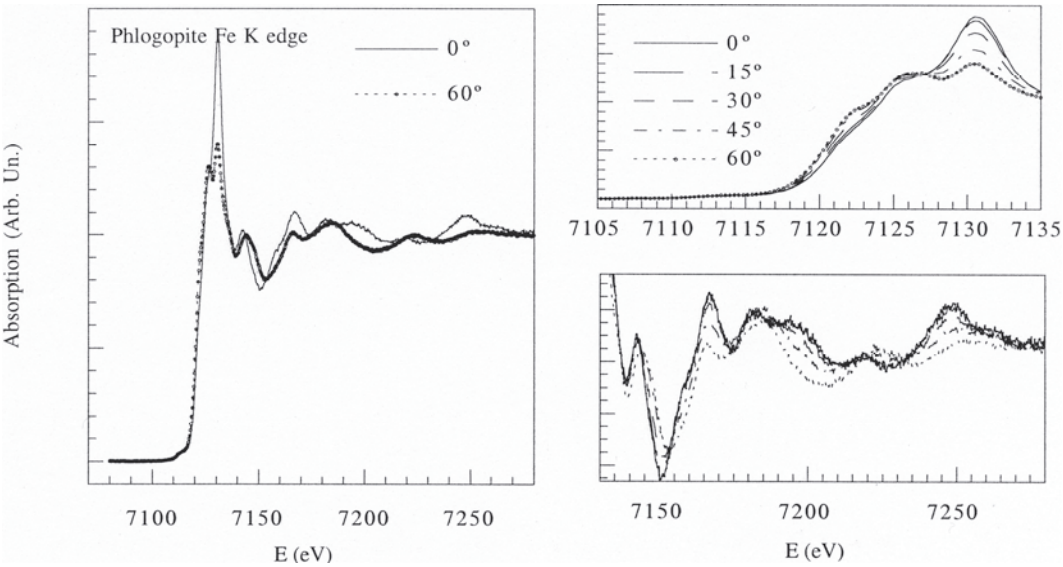

Figure 8. Changes in a Franklin phlogopite Fe *K*-edge spectrum due to changing the orientation of the same crystal blade against the impinging, horizontally-polarized synchrotron radiation beam. In the right panel a magnified view of the changes undergone as a function of the α rotation angle by the edge and FMS regions (top) and by the IMS region (bottom).

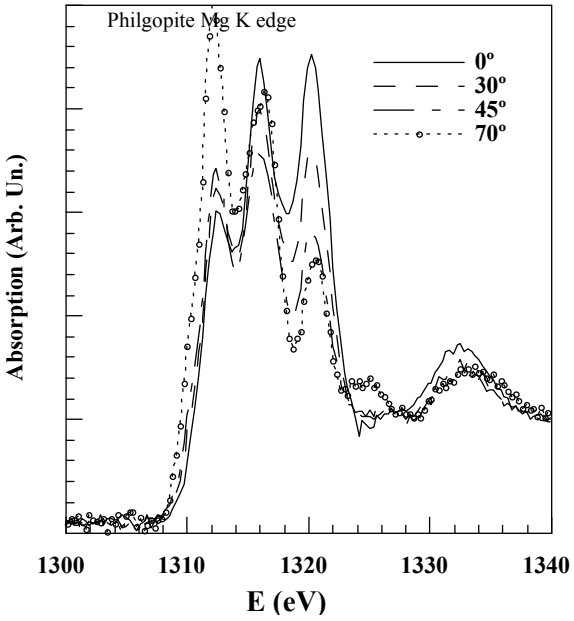

Figure 9. Changes in the FMS region of a Franklin phlogopite Mg *K*-edge spectrum due to changing the orientation of the same crystal blade against the impinging, horizontally-polarized synchrotron radiation beam.

imply displacements in the peak positions from 0 up to 5 eV, and variation in the intensities by as much as 50%, with even reversals in the intensity of the edge top (Fig. 9) or appearance viz. disappearance (Fig. 11) of certain features. Most commonly, these changes occur gradually and trend always in the same direction, thus demonstrating their dependence upon the gradual rotation applied to the crystal. In turn, this rotation mostly reflects changes in the lengths of the bonds lying in the polarization plane, excited in the photoabsorption process, or in the lengths of multiple-scattering paths which are also probed in that geometry. Such spectral changes affect both the FMS and IMS regions, thus showing their dependence mostly upon the geometry of the section of the crystal that is being scanned by the synchrotron beam, as cosα. However, unexpected changes such as the one at the white-line in the phlogopite Mg *K*-edge spectrum (Fig. 9), or the sudden

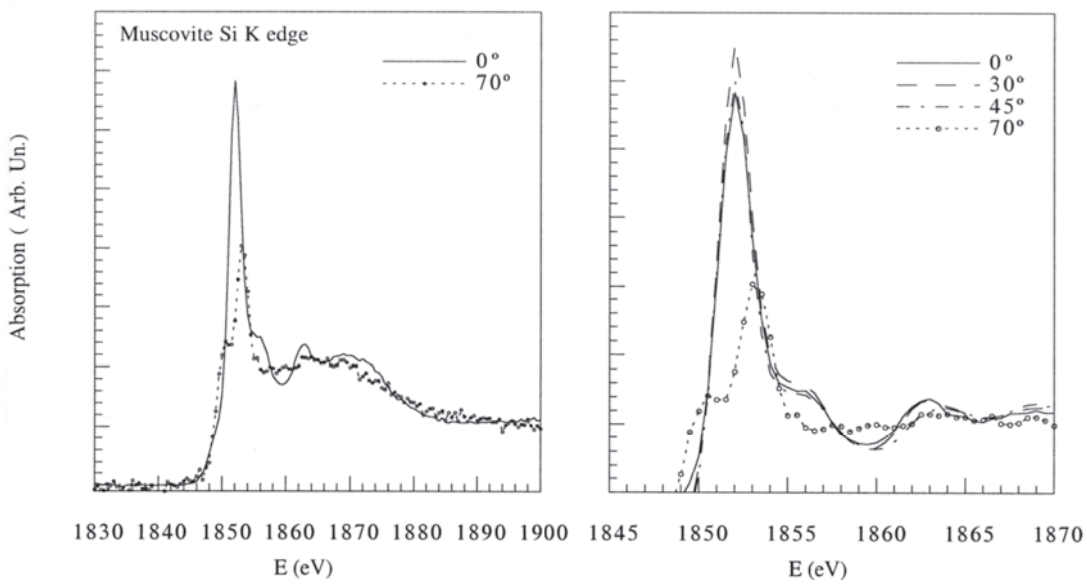

Figure 10. Changes in an Antarctica muscovite Si *K*-edge spectrum due to changing the orientation of the same crystal blade against the impinging, horizontally-polarized synchrotron radiation beam. In the right panel a magnified view of the changes undergone by the edge and FMS regions.

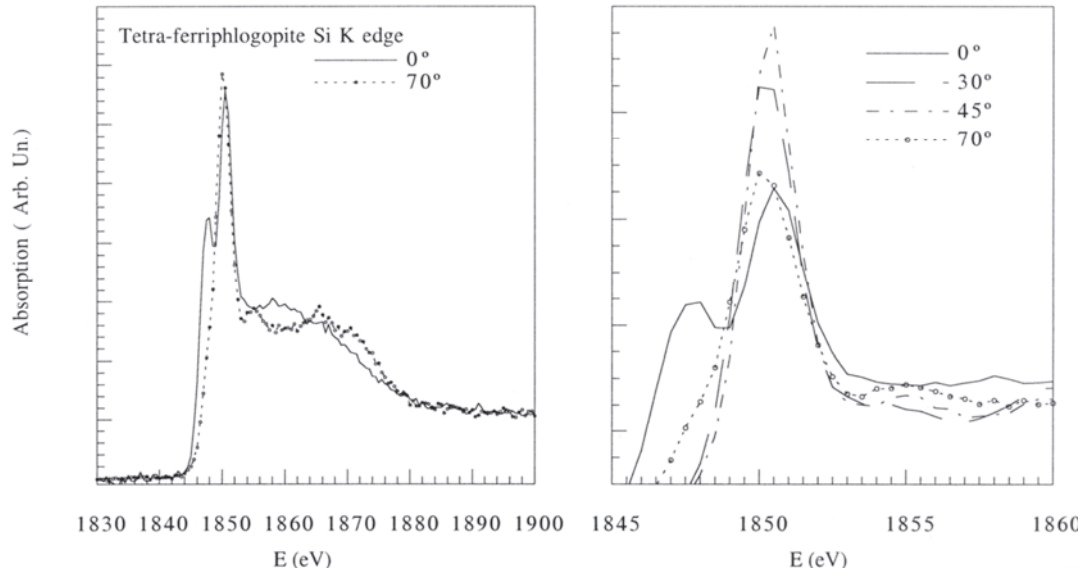

Figure 11. Changes in a Tapira tetra-ferriphlogopite Si *K*-edge spectrum due to changing the orientation of the same crystal blade against the impinging, horizontally-polarized synchrotron radiation beam. In the right panel a magnified view of the changes undergone by the edge and FMS regions.

appearance of a new low-energy peak, as in the muscovite Al and Si *K*-edge spectra (Figs. 7 and 10) and in the tetra-ferriphlogopite Si *K*-edge spectrum (Fig. 11), demonstrate the possibility that the electronic properties of the absorbing atom are also involved. We have to underline here that this interpretation of the near-edge structure is fully equivalent to the interpretation that is based on local geometrical distributions, such

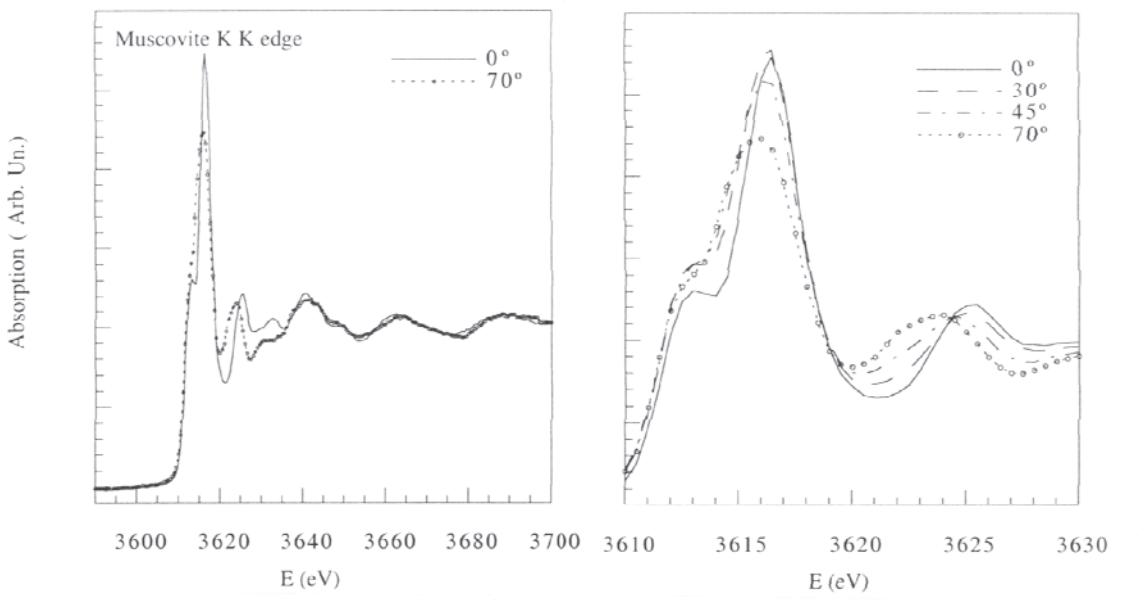

Figure 12. Changes in an Antarctica muscovite K *K*-edge spectrum due to changing the orientation of the same crystal blade against the impinging, horizontally-polarized synchrotron radiation beam. In the right panel a magnified view of the changes undergone by the edge and FMS regions.

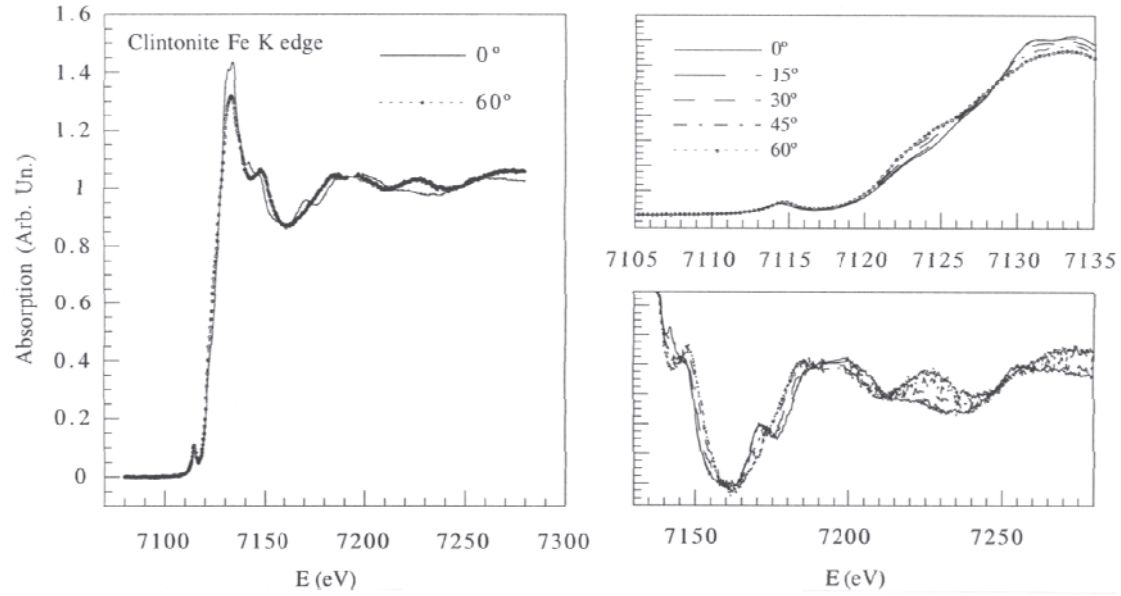

Figure 13. Changes in a Lago della Vacca clintonite Fe *K*-edge spectrum due to changing the orientation of the same crystal blade against the impinging, horizontally-polarized synchrotron radiation beam. In the right panel a magnified view of the changes undergone by the edge (top) and IMS regions (bottom).

as those expected when the different local atomic distributions in the micas are being compared.

To summarize, in order to obtain XANES spectra that may be meaningfully compared, we recommend orienting the sample, when a single crystal, always at the same angle of rotation $\alpha = 54.7°$. This is essentially the same conclusion reached by Manceau et al. (1998) for the self-supporting clay films they experimentally investigated by

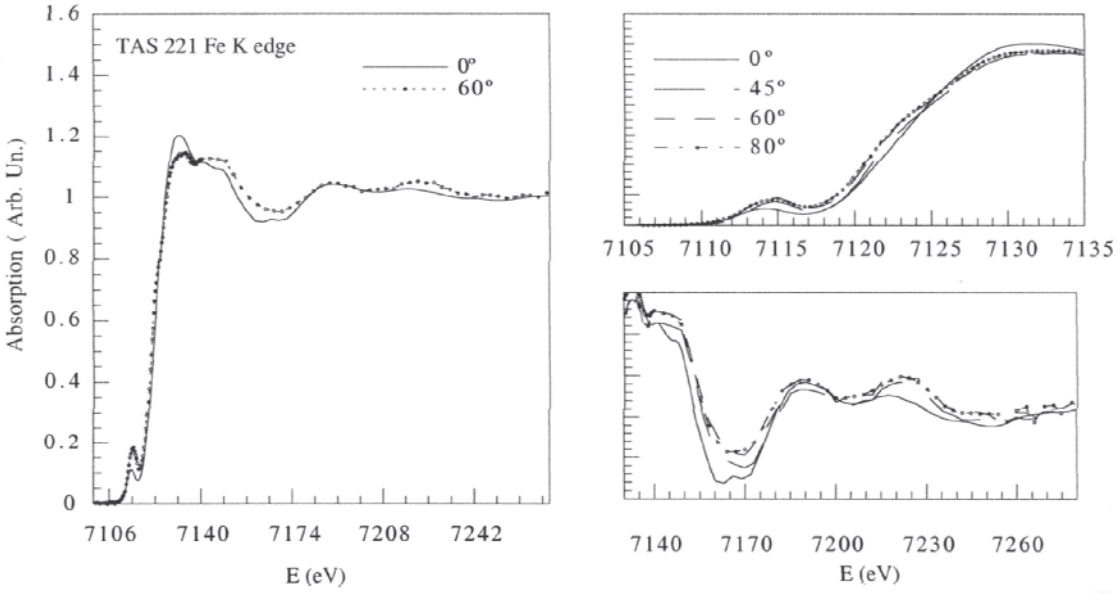

Figure 14. Changes in a Tapira tetra-ferriphlogopite Fe *K*-edge spectrum due to changing the orientation of the same crystal blade against the impinging, horizontally-polarized synchrotron radiation beam. In the right panel a magnified view of the changes undergone by the edge (top) and FMS and IMS regions (bottom).

polarized EXAFS and theoretically interpreted by performing full multiple-scattering calculations. Furthermore, we also recommend recording a full XAS spectrum of the same sample, after grinding it and settling in water for precisely determined times so as to obtain a well-classified powder possibly in the grain size range 1 to 2 μm.

Dyar et al. (2000) used a different method of studying the orientation effects on the pre-edge region of Fe-bearing micas, with similar results. In that study, the micro-XANES probe at the National Synchrotron Light Source (NSLS), Brookhaven, NY, was used, allowing a beam size of 10 × 15 μm. Because the beam is smaller, samples on the order of 30 × 30 × 100 μm (orders of magnitude smaller than those used by other workers) could be studied, and concerns about sample homogeneity lessened. Each crystal was oriented with its cleavage perpendicular to a glass thin section, and then UV-hardening epoxy was used to maintain it in that geometry. The mica+epoxy was removed from the thin section, and two mutually parallel faces were polished on each sample perpendicular to cleavage (though in an unknown orientation relative to the **a** and **b** axes: see Fig. 15). This preparation permitted acquisition of spectra in two important directions

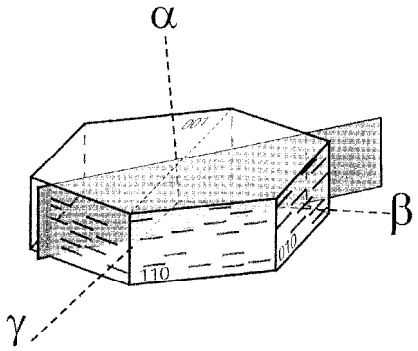

Figure 15. Optical orientation of a model mica crystal showing the random position of the thin section cut across cleavage and used for microXANES measurements (Dyar et al. 2001).

perpendicular and parallel to cleavage by simple rotation of the sample. A further advantage of this method is that parallel studies of the optical and IR absorption spectra of the identical crystals could be made. In more recent work (Dyar et al. in prep.) single crystals were analyzed while mounted on goniometer heads, so the beam could be polarized along the X, Y, and Z optical orientations.

As with the work of Mottana et al. (in preparation), changes in peak intensity and, to a lesser extent, energy, were observed by Dyar et al. (2001) as a function of sample orientation. At the main edge, the difference in the intensity of the highest energy peak relative to the other prominent peak or peaks is generally greatest when the synchrotron beam is polarized in the direction of the cleavage plane, with a few exceptions. In the pre-edge region, intensity variations were also observed, but the maxima and minima were not necessarily parallel or perpendicular to cleavage, and the orientation at which maximum intensity occurred was different for various samples. This implies that there are variations in peak intensity not only perpendicular and parallel to the mica cleavages, but also within the sheets themselves as a function of orientation with respect to the unconstrained position in the XY plane. Such a conclusion is not surprising in a monoclinic mineral species: the XANES probe is sampling different bonds at different orientations relative to noncentrsymmetric Fe sites (Dyar et al. 2001; in prep.).

Spectrum fitting. In standard XAS experiments, signal to noise (S/N) ratios in the range 10^3~10^4 can be achieved. However, to fully enhance XANES potentials, these are not enough, especially in the soft-X-ray energy range where such ratios are only achieved after a perfect preparation of the sample. Consequently, with a lower S/N ratio, the best understanding of XANES critically depends upon a careful fitting of the experimental spectrum during which no fine details get lost.

The standard procedure in XAS spectrum analysis follows two steps: the experimental spectrum is (1) corrected for background contributions from lower energy absorption edges by linear or polynomial fitting of the base line, then (2) normalized at high energy, i.e., close to the upper end of the XANES region at an energy position where no obvious features can be seen. In addition, for pre-edge analysis the contribution of the absorption jump is subtracted by an arctangent function. This procedure leaves a profile of the entire *K*-edge region that consists of a number of features, occasionally partially superimposed, that can be either evaluated visually or fitted by Gaussian or Lorentzian curves. The numerical values of the fitted curves (energy and intensity, with errors and significance bars) can then be used as solid data for interpretation. This standard procedure assures accuracy in energy position ±0.1 eV for the pre-edge, and ±0.03 eV for all other regions of the XANES spectrum. Both values are well within resolution, which increases with energy from ca. 0.3 to ca. 1.5 eV on going from the Na *K*-edge to the Fe one (Schaefers et al. 1992). Accuracy in the intensity measurements is estimated to be better than 10%. However, such intense structures as the "white line" are affected mainly by the harmonics content.

At all synchrotron sources, a step preliminary to all this standard procedure consists of calibrating the energy positions of all peaks against standards (usually metal foils). An alternative way is to calibrate them against a “glitch”, i.e., a spurious absorption at constant energy in the spectra that is due to a planar defect present in the monochromator crystal (cf. Wong et al. 1999, for YB_{66}). When high thermal loads heat the monochromator crystals, a further systematic correction is applied that takes into account the decrease of the ring current (and heat load) with time.

As a matter of fact, in most mica studies a careful fitting procedure is seldom applied, and the “fingerprinting” method of evaluation is still predominant (Table 1). A

recent improvement in the fitting procedure is based upon a novel software (Benfatto et al. 2001). However minor the error induced by such evaluation may be, any concomitant carelessness in taking into account orientation effects would, at the end, result in crowding the literature with spectra useless for interlaboratory comparisons.

Systematics

XAS studies on micas: a catalogue. Table 1 lists all XAS studies carried out on micas that could be retrieved in the relevant literature. They are presented in the alphabetical order of the di- and tri-octahedral mica species nomenclature approved recently (Rieder et al. 1998) and are further subdivided on the basis of the investigated atom.

Almost all investigated samples are natural and are therefore intermediate in composition. However, some of them are close enough to end member compositions as to make it possible to classify them accordingly. Only seven true end members corresponding to natural mica species have been studied so far by XAS, i.e., the Tapira tetra-ferriphlogopite (Giuli et al. 2001) and the six synthetic micas investigated by Mottana et al. (1997). Even all other synthetic micas (Osuka et al. 1988 1990; Sakane et al. 1997) are intermediate, as they are doped crystals obtained for technological purposes. Furthermore, among the synthetic micas quite a few have no natural counterpart (Soma et al. 1990; Han et al. 2001). XAS studies on otherwise insufficiently characterized samples, or on samples with composition being complex solid solutions from the crystal-chemical viewpoint, are listed at the bottom of Table 1, in the section that accounts for the approved series names (cf. Rieder et al. 1998 Table 4).

The first XAS spectra ever recorded on micas were those by Brytov et al. (1979) at the Si and Al *K* edges. However, as all these spectra were recorded in the late 1970s and early 1980s using a conventional X-ray tube as the source, they are practically useless for present-days studies because of the limited resolution: in practice, only the general shape is worth examining (e.g., Jain et al. 1980 Fig. 1). Nevertheless, these early attempts deserve to be remembered, for both the pioneering effort they record and their historical significance.

The earliest synchrotron-activated experimental XAS spectrum for any mica was Calas et al.'s (1984) chromium muscovite at the Cr *K* edge. Although noisy, particularly in the pre-edge region, this spectrum satisfactorily compares with the recent spectrum of a similar mica at the same edge (Brigatti et al. 2001; see below), thus suggesting not only the high level of technical skill of the operators, but also that comparison of power spectra collected at very different times and on widely different synchrotron storage rings can be confidently made, provided the basic requirements of energy calibration and background subtraction were carefully applied (see above).

Occasionally, mica has been used also to support epitaxially-grown layers that have been investigated by XAS (e.g., Blum et al. 1986; Drozdov et al. 1997). Although reported in Table 1, these XAS studies actually do not belong to mica studies. Finally, there has never been a spectrum published so far but those presented above to which the above-given precautions on orientation effects were applied (see also Dyar et al. 2001 and in prep.). Even the spectra that will be described in the following were obtained on ground powders, presumed to be homogeneous in their grain-size and randomly oriented, but never tested for those conditions.

Determination of the oxidation state. Determining the effective charge on the absorbing atom from the chemical shift of the X-ray absorption threshold is a fundamental issue for XANES. However, a direct measure of the "ionization threshold" or "continuum threshold" (i.e., the energy at which the electron is excited in the

continuum: e.g., the Fermi level in metals) is not possible because of the lack of any signature of it. Therefore, XANES is not a direct probe of core-level binding energy as other methods are (e.g., XPS or ESCA). However, there is evidence in both gas molecules and solid compounds that the energy shift of the first bound excited state at the absorption threshold follows the binding energy shift of the core level. Moreover, a linear dependence between core-level binding energy and atomic effective charge has been measured (Belli et al. 1980). By contrast, no linear relationship between the measured shift of the first strong multiple-scattering resonance and the effective atomic charge on the ion exists. The energy of multiple-scattering resonances is strongly dependent on interatomic distance, so their chemical shifts are much larger than that of the core excitation. Actually, the variation of the effective charge on an atom is often increased and a linear correlation with core-level binding energy indeed exists; however, this effect is always system-dependent. Moreover, within the same structure any correlation among the parameters of the potential is certainly confined only to small changes of the interatomic distances (e.g., less than 10%).

Correct identification of the oxidation state of 3*d* transition metals is indeed important, but the quantification of the oxidation ratio is even more important in the case of potentially multivalent minerals such as the micas, a group where the number of elements occurring with more than one oxidation state is significant (Fe, Mn, Cr, V and possibly Ti: cf. Table 1) and their amounts may be so large as to even become essential and determine new end members. All transition element *K*-edge spectra display a pre-edge (Belli et al. 1980) and, mostly, all features of the pre-edge are strong enough to be easily recorded experimentally. Position and intensity of the peaks occurring in the pre-edge region can be reliably used to determine the oxidation state(s) of the absorbing atom (e.g., Waychunas 1987). However, as already seen (Fig. 2, above), coordination too plays a role, so that care must be made in discriminating the two effects, and to this purpose spectra need to be properly deconvoluted.

As discussed above, the energy position of the peaks in the pre-edge region may be directly related to the increase in the oxidation state of the absorber atom: e.g., the pre-edge feature of Fe^{3+} is generally ca. 2~3 eV higher in energy than the corresponding feature for Fe^{2+} (Waychunas et al. 1983; cf. Petit et al. 2001). The amount of such a "chemical shift" is different for the different transition elements, and depends on the final state reached by the electron. Implicitly, this weakens the possibility of reliably determining the oxidation state of a given atom when it occurs in different coordination sites of the same compound. However, when a significant part of the atom occurs in a tetrahedrally-coordinated site, the relevant pre-edge is strongly intensified owing to *d-p* mixing, and the determination of the oxidation state of the tetrahedral atom is made fairly easy to measure: e.g., amounts of Cr^{3+} in tetrahedral coordination as small as 0.5% could be detected even in the presence of a significant amount of Cr^{3+} in octahedral coordination (Brigatti et al. 2001; see below). Consequently, subtraction of the tetrahedrally-coordinated component can be made. The residual pre-edge spectrum of the octahedrally-coordinated atoms is then de-convoluted into its components to determine their oxidation state(s).

Bajt et al. (1994 1995) and Sutton et al. (1995) have pushed the practice of pre-edge examination further to reach an effective quantification of the oxidation states for Fe, the atom which most frequently occurs in two oxidation states in the same site of minerals. They have developed, and Galoisy et al. (2001) and Petit et al. (2001) have recently improved upon, a procedure that makes use of the known positions of pre-edge peaks of Fe *K*-XANES spectra in mineral standards to fit a calibration line giving the $Fe^{3+}/\Sigma Fe$ ratios of various minerals (Fig. 16).

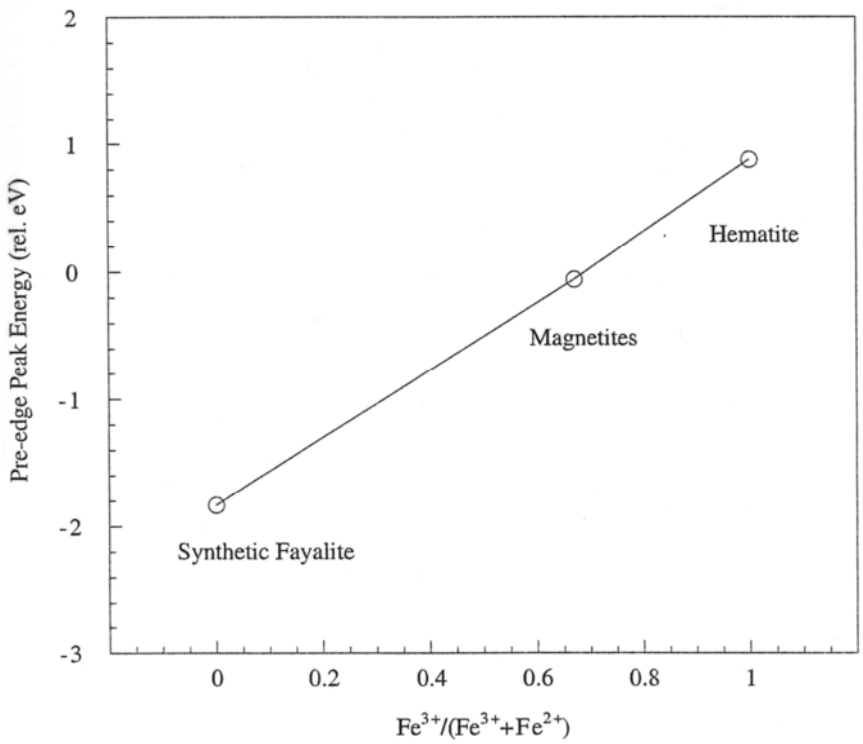

Figure 16. Plot of "pre-edge peak energy" vs. "$Fe^{3+}/\Sigma Fe$" for well characterized standards. The trend is linear with a correlation coefficient of 0.99 (after Sutton et al. 1995, p. 1465, Fig. 3).

However, extensive additional work by Dyar et al. (2001) on suites of Fe^{3+} and Fe^{2+} end members confirms that the energies of the end-member pre-edges vary considerably for several different mineral groups, and thus no single mineral species can be used to model all cases of any type of Fe (Fig. 17). Because different mineral groups have variably distorted coordination polyhedra, use of mineral group-specific standard end members will ultimately be necessary to interpret pre-edge positions assigned to different transitions. Examples of using this method to determine of the $Fe^{3+}/\Sigma Fe$ ratios of a number of rock-forming micas are given elsewhere (Dyar et al. 2001).

Determination of local coordination geometry. The position and intensity of the peaks in the pre-edge region do not solely depend upon the oxidation state of the absorber transition metal, but also upon the shape of the site (coordination polyhedron) where the absorber is located in the structure (Calas and Petiau 1983). An increase in coordination number provokes a positive energy shift, while the intensity of the peak is proportionally reduced (Waychunas et al. 1983).

The first attempt at using the pre-edge features to determine quantitatively site geometry is Waychunas' (1987) for the Ti *K*-edge of a suite of silicate and oxide minerals, including a biotite from Antarctica. He fitted Gaussian features to the entire edge region, and found that individual features are insensitive to changes in the Ti-O bond length, but sensitive to valence, with Ti^{3+} at ca. 2.0 eV lower energy than Ti^{4+}. Moreover, the intensity of the second pre-edge feature at ca. 4969 eV turned out
to be sensitive to both octahedral site distortion and to presence of tetrahedral Ti^{4+}. A correlation was found for silicates between intensity and bond-angle variance σ^2 in the octahedral Ti site, and for biotite σ^2 could be quantified to be ca. 30 deg^2, in fair agreement with the value computed from the X-ray diffraction crystal structure determination (Ohta et al. 1982). Cruciani et al. (1995) essentially followed the same

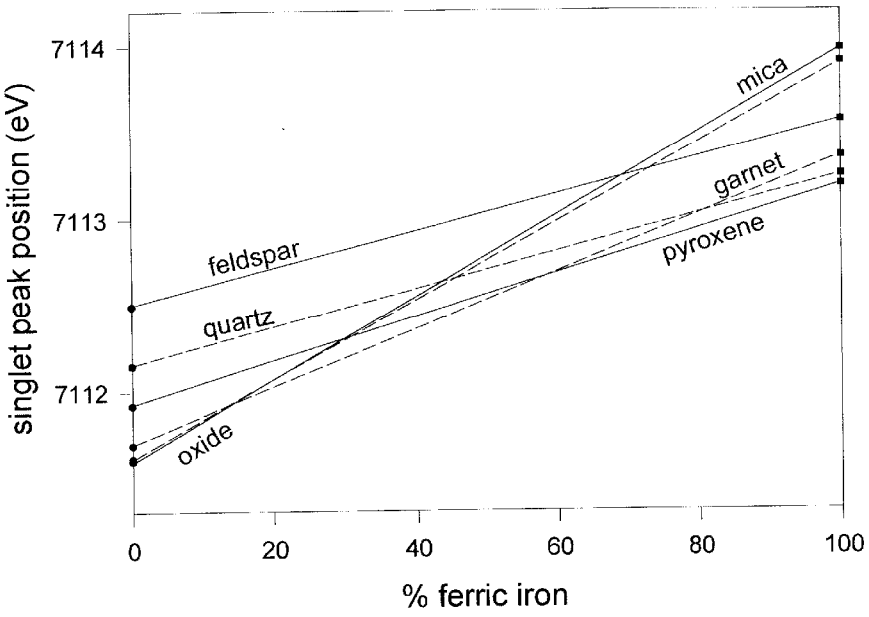

Figure 17. Variation of the absolute pre-peak energy vs. Fe^{3+} content in the end-members of several mineral groups; after Delaney et al. (in preparation).

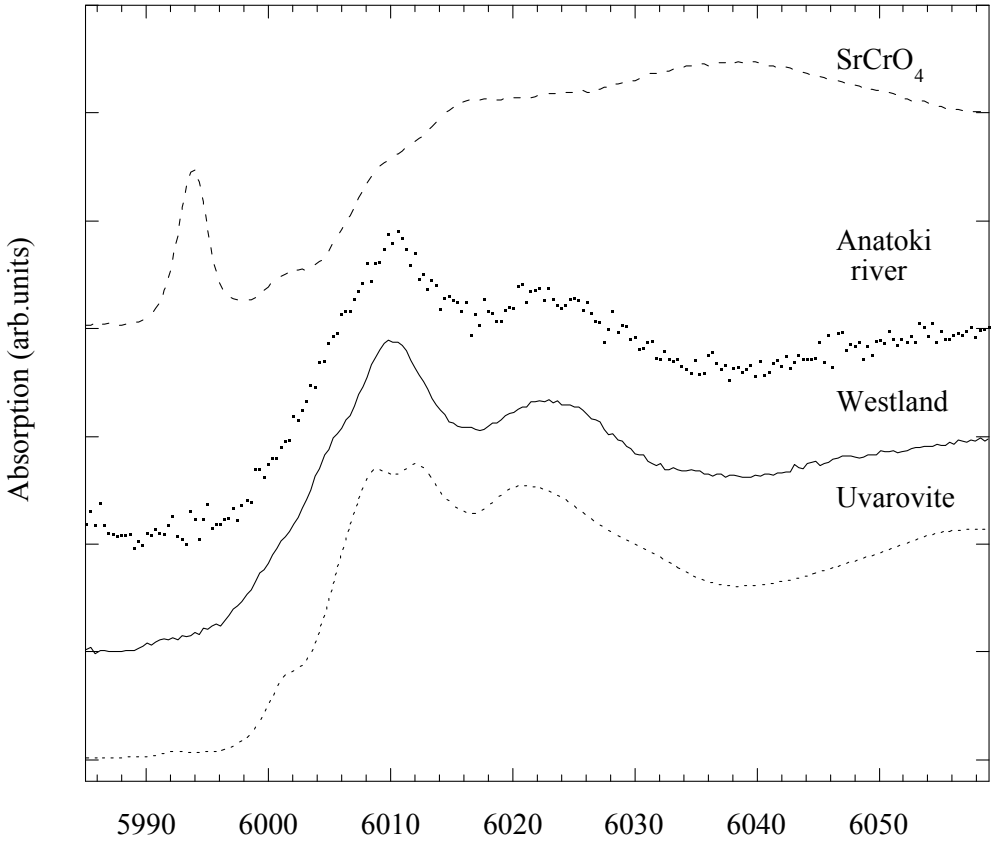

Figure 18. Experimental Cr *K*-edge spectra for the Anatoki River and Westland chromium muscovites, a synthetic $SrCrO_4$ standard for tetrahedral Cr^{6+} (top) and an Outukumpu uvarovite standard for octahedral Cr^{3+} (bottom). See text for discussion (Brigatti et al. 2001, Fig. 6).

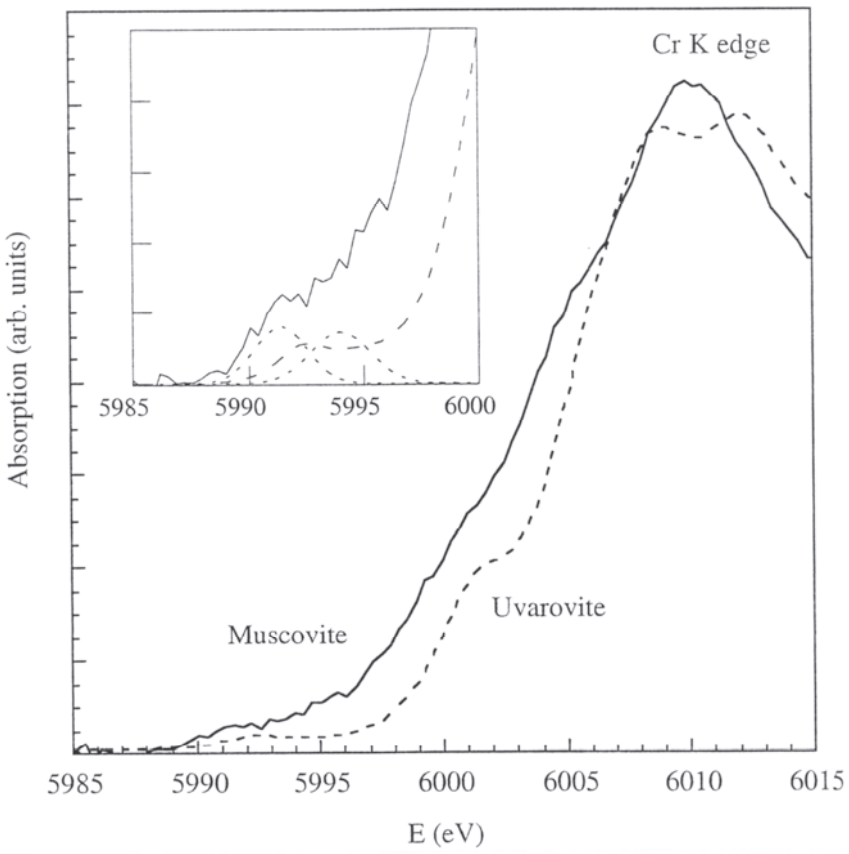

Figure 19. Pre-edge fit of the Westland chromium muscovite Cr *K*-edge spectrum of Figure 18 and (inset) its de-convolution in two Gaussian components (Brigatti et al. 2001 Fig. 7).

procedure when trying to determine the $^{[4]}Fe^{3+}$ contents of a series of natural phlogopites, but came to a purely speculative result owing to the insufficient resolution of the monochromator crystal and the extremely low amount of sample available.

As an example of successful evaluation, we report the case of two chromium muscovites worked out by Brigatti et al. (2001) at the Cr *K* pre-edge; the procedure they followed is the one developed by Peterson et al. (1997) for oxides. The Anatoki River and Westland chromium muscovites Cr *K*-edge spectra were compared with a synthetic $SrCrO_4$ standard, for tetrahedral Cr^{6+}, and a natural uvarovite, for octahedral Cr^{3+} (Fig. 18). The Anatoki River muscovite Cr *K*-edge spectrum proved to be too noisy for further evaluation, but the Westland one, after subtraction of the edge contribution by a pseudo-Voigt function, had its pre-edge resolved in two Gaussian components: at 5991.3 eV and 5994.0 eV, respectively (Fig. 19). The second Gaussian component appears in the experimental spectrum only as a skew tail at the end of the pre-edge, owing to interference with the rapidly rising slope leading to the edge. However, after subtracting this interference, it can be reliably measured for both energy and intensity. The evaluation step that follows involves interpretation. If the second-component intensity is assumed to be the same as that of the single, symmetrical Gaussian pre-edge feature of a $SrCrO_4$ standard in which the Cr^{6+} is entirely in tetrahedral coordination, then it can be appraised that amount of $^{[4]}Cr$ in muscovite, if any, cannot exceed 0.4-0.5% of total Cr (cf. Lee et al. 1995). By contrast, if both Gaussian components are considered to be due to $^{[6]}Cr^{3+}$, as in the uvarovite standard, and interpreted as a way to measure the distortions of the muscovite octahedral sites where Cr^{3+} is possibly hosted, then their relative

intensities (1.3 and 1.2% nau [= normalized absorption units]) show that these two sites are very similar. Indeed, this is nothing more than an extension to Cr of the method for quantitatively determination of site distortion for octahedra centered by Ti^{4+} calibrated by Waychunas (1987).

In the case of the already-mentioned Fe *K* pre-edge of tetra-ferriphlogopite, where Fe^{3+} is entirely in the tetrahedral site, the pre-edge is twice as strong and shifted to higher energy (ca. 2 eV) relative to annite, where Fe is mostly in the octahedral site (Fig. 2). This apparent irregularity can be explained by comparing the sharp single peak of tetra-ferriphlogopite, a synthetic endmember, and the broad, probably double peak of the Pikes Peak annite, the Fe of which is entirely octahedral, but partly Fe^{2+} and partly Fe^{3+}. Clearly, the oxidation effect is more important than the coordination effect in determining the position of the Fe *K* pre-edge. However, the strong intensity of the tetra-ferriphlogopite peak also suggests that its Fe is constrained in a more tightly-bound coordination polyhedron than the annite one. Note, however, that there is an underlying problem in the pre-edge region that needs a more careful evaluation, and not only in these systems: this problem is the amount of quadrupolar effects present (see Giuli et al. 2001, for additional evaluation).

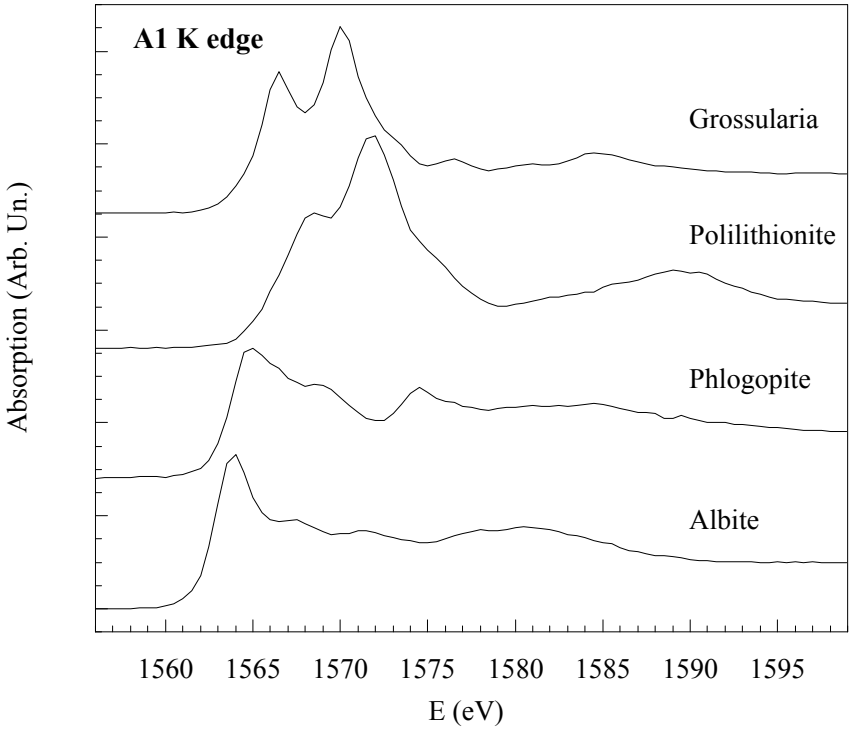

Figure 20. Shift of the white-line in the FMS region of the Al *K*-edge spectra of two synthetic micas as a result of two different coordination geometries: in phlogopite the Al atoms are entirely in a tetrahedral site geometry, and in polylithionite in an octahedral site geometry, as they are in the reference albite and grossular natural standards, respectively (Mottana et al. 1997, Fig. 3).

Coordination geometry also plays a role in shaping the FMS region of a XANES spectrum. This effect was clearly documented for the Al *K* edges of certain synthetic micas by Mottana et al. (1997), who showed that there is a shift of at least 2 eV between $^{[4]}$Al as in phlogopite and albite, and $^{[6]}$Al as in polylithionite and grossular (Fig. 20). Moreover, they found that it is possible, although difficult, to recognize the concomitant presence in the spectra of two white-line features arising from contributions of the same atom occurring in two different geometries ($^{[4]}$Al and $^{[6]}$Al in zinnwaldite and

preiswerkite: Mottana et al. 1997 Fig. 4). Thus, the FMS region of the XANES spectrum of a mineral with Al in two coordinations can be seen as the weighted combination of the contributions arising from the two Al atoms, although the general appearance of the spectrum (and its ensuing evaluation) is somewhat blurred by next nearest neighbor effects due to the presence of other atoms in the same sites substituting for the absorber Al (cf. the muscovite vs. bityite spectra: Mottana et al. 1997 Fig. 4).

In the following we will document visually and sparingly comment upon a series of XANES spectra obtained at different *K* edges for the powders of a number of natural micas close to the end members. The present state of our investigation, which is still under way, compels us to defer to a later moment for drawing conclusions (Mottana et al., in preparation): micas are no simple systems, and XAS literature is already cluttered by faulty reasoning and wrong conclusions reached when hastily evaluating even simpler systems!

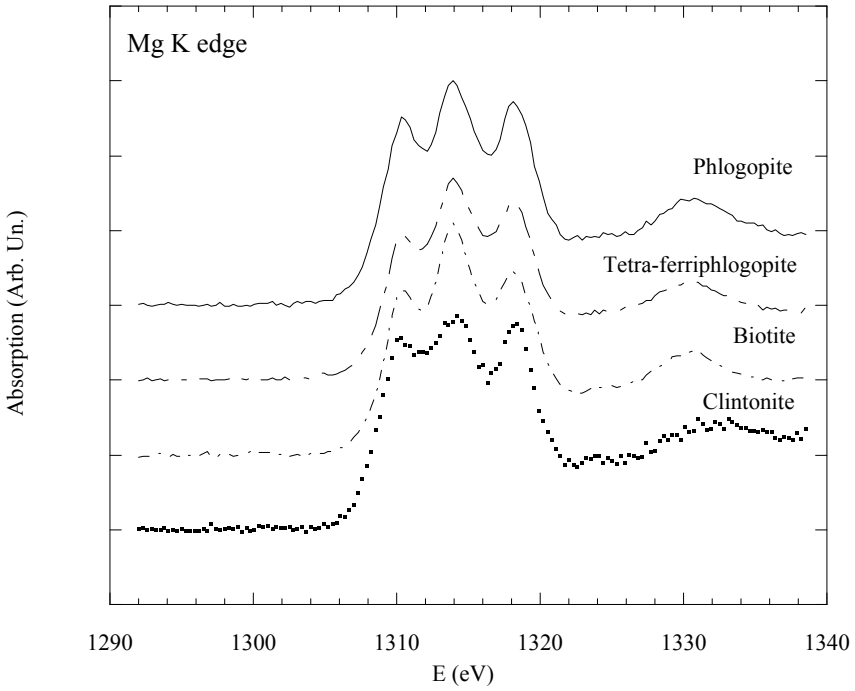

Figure 21. Experimental Mg *K*-edge spectra for the powders of four natural tri-octahedral micas.

Figure 21 shows the experimental Mg *K*-edge spectra of three tri-octahedral micas (phlogopite, tetra-ferriphlogopite, and biotite) and one brittle mica (clintonite). All spectra are very similar and have no pre-edges, as magnesium is not a transition element. The FMS regions consist of three features, like the *K* edge of talc (Wong et al. 1995). However, the relative intensities of the three features differ significantly among the four spectra suggesting that there are substantial differences in the local order of their Mg that may be resolved via comparison with spectra taken for other absorbers. Note, moreover, that the three features in the clintonite spectrum are possibly doubled.

Figure 22 shows the experimental Al *K* edge spectra of three tri-octahedral micas (phlogopite, annite, biotite) and one di-octahedral mica (muscovite). Again, Al is not a transition element, therefore the spectra have no distinct pre-edges. The FMS regions are apparently simpler than the ones occurring in the Mg *K*-edge spectra above, but in fact

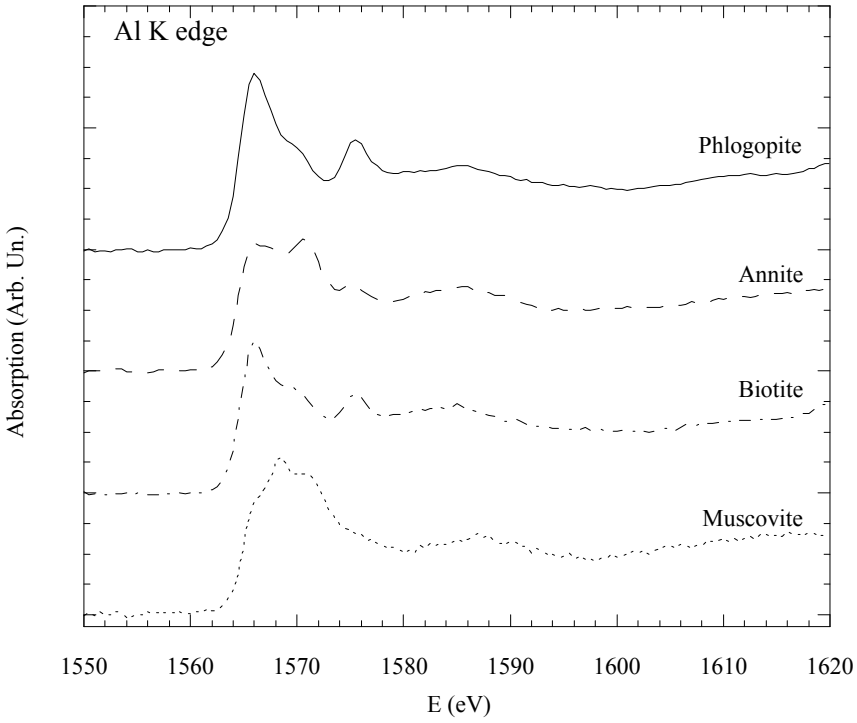

Figure 22. Experimental Al *K*-edge spectra for the powders of three natural tri-octahedral and one natural di-octahedral mica.

they contain the same three features, although with strongly different intensities and energies (cf. Mottana et al. 1999). Possibly, the fact that non-precisely oriented powders were used affects the recorded features (cp. this muscovite spectrum with that in Fig. 7). The IMS regions are poor in features, but they display shifts and relative differences that are enormous, considering the similarity of the local structures that originate such differences. The significant role of the outer shells around the Al absorber appears to be well depicted here, but it will create great problems when interpreting the spectra from a quantitative viewpoint.

Figure 23 shows the experimental Si *K*-edge spectra of five micas: four tri- and one di-octahedral one. Nowhere is there a pre-edge, and the entire XANES spectrum is dominated by the strong white-line of Si in tetrahedral coordination (cf. Li et al. 1994; Li et al. 1995a). The regions in between FMS and IMS (inset) undergo subtle but significant variations as a result of changes in the local and medium-range ordering occurring in the relevant structures for the volumes that surround the Si tetrahedra. Such variations may also occur in the energies of certain peaks, but this variation is also certainly due to the tri- vs. di-octahedral structure of the investigated mica (inset: cf. muscovite with the other micas).

The experimental K *K*-edge spectra of the same five micas are shown in Figure 24. These XANES spectra are rather complex, both to record experimentally and to reckon with. The FMS regions have no strong white-lines, and only small differences show up in the intensities of their IMS regions (inset). However, their analysis suggests that the K coordination number is less than the expected 12, possibly 8 or even 6. In a case like this, only XANES simulations by the multiple-scattering code may be able to reveal safely the actual site geometry around the potassium atom.

Finally, Figure 25 shows the experimental Fe *K*-edge spectra of two trioctahedral

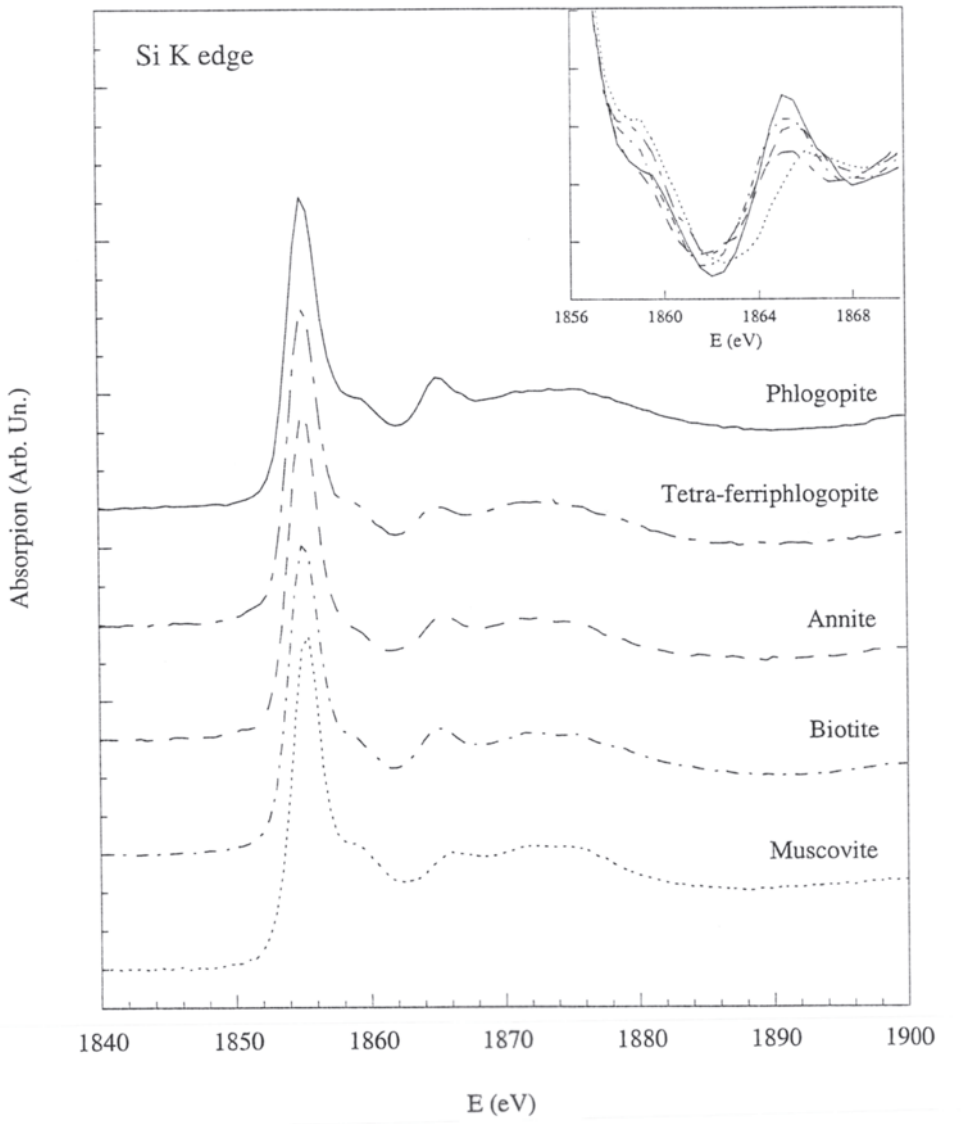

Figure 23. Experimental Si *K*-edge spectra for the powders of five natural micas. The strong differences displayed by a portion of their FMS and IMS regions is shown as inset.

micas (biotite and tetra-ferriphlogopite) and one brittle mica (clintonite). Iron is a transition element, therefore all spectra exhibit significant pre-edges (inset), each one of them having properties of its own. In particular, the tetra-ferriphlogopite pre-edge is a singlet (cf. Fig. 2), as is the clintonite one, but at 1 eV lower energy. Fe is tetrahedrally-coordinated in both micas, but in the former one it is Fe^{3+} and in the latter one an additional contribution arising from Fe^{2+} is likely. The biotite pre-edge is weak, because it mostly arises from octahedral Fe^{2+}. The three pre-edges require a deconvolution of the same sort as the one previously demonstrated for the Cr pre-edge of muscovite (Fig. 19) in order to reveal all the information they contain. The FMS regions of these spectra are dominated by the Fe white-line, which undergoes energy variations accounting for differences in both coordination and oxidation state. The presence of significant variations in the medium- to long-range ordering occurring in these mica structures is made evident by their greatly different IMS regions (and also by their EXAFS regions: cf. Giuli et al. 2001).

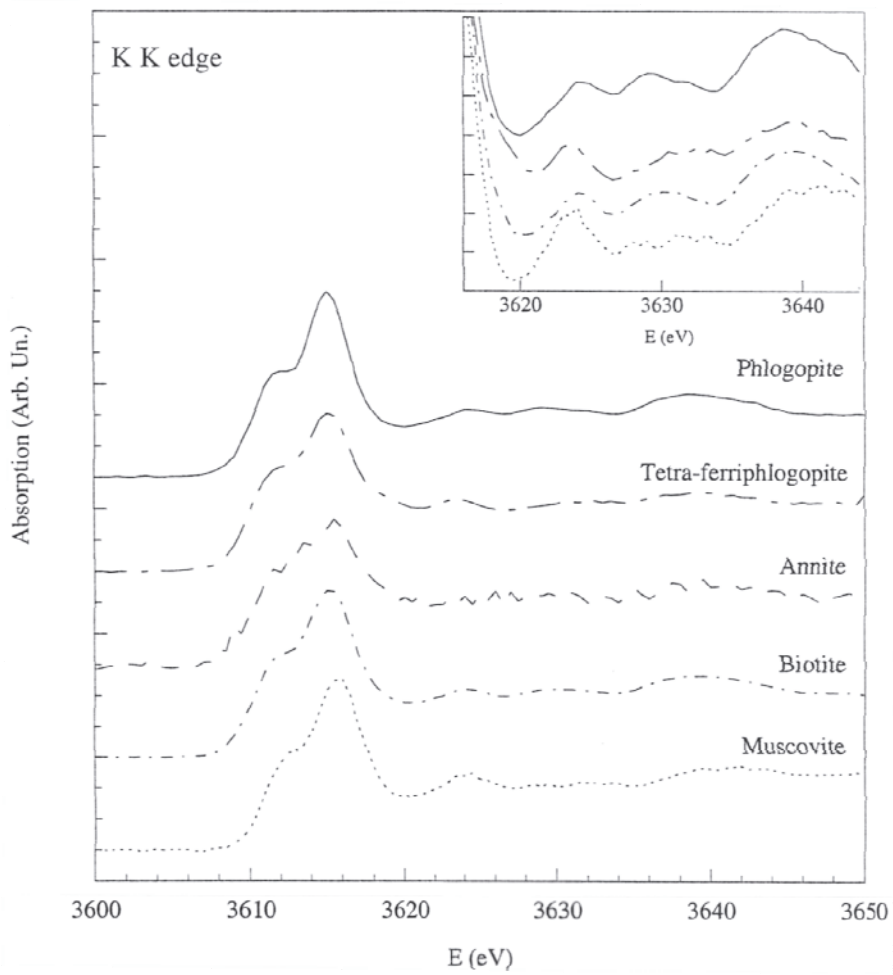

Figure 24. Experimental K *K*-edge spectra for the powders of five natural micas. The strong differences displayed by a portion of their FMS and IMS regions are shown as an inset.

ACKNOWLEDGMENTS

Our XAS work on minerals has enjoyed the support of numerous suggestions, discussions and contributions in many stages and levels over a number of years, the five more recent ones dedicated mostly to the micas. We thank all these colleagues, since it is by this form of synergy that we could carry out and develop our project over the years. A special thank goes to Maria Franca Brigatti, Jesús Chaboy, Paola De Cecco, Giancarlo Della Ventura, Gabriele Giuli, Antonio Grilli, Cristina Lugli, Jeff Moore, Takatoshi Murata, Eleonora Paris, Marco Poppi, Agostino Raco, Jean-Louis Robert, Claudia Romano, Michael Rowen, Francesca Tombolini, Hal Tompkins, Curtis Troxel, Joe Wong, Ziyu Wu and all others who allowed us to use for this review some of the data recorded together during painstaking sessions at the source. Most experimental XAS was carried out at SSRL, which is operated by Stanford University on behalf of D.O.E. Furthermore, M.D.D. acknowledges the insight and assistance of her collaborators at the N.S.L.S., Brookhaven National Laboratory: Jeremy Delaney, Tony Lanzirotti and Steve Sutton. Financial supports for our experimental work and for its evaluation and interpretation were granted by M.U.R.S.T. (Project COFIN 1999 "Phyllosilicates: crystal-chemical, structural and petrologic aspects"), C.N.R. (Project 99.00688.CT05 "Igneous and metamorphic micas"), and I.N.F.N. (Project "DAΦNE-Light") in Italy, and by N.S.F.

EAR-9909587 and EAR-9806182, and D.O.E.-Geosciences DE-FG02.92ER14244 in U.S.A. Critical readings by C.R. Natoli and a unknown referee improved the quality of this paper in a substantial manner.

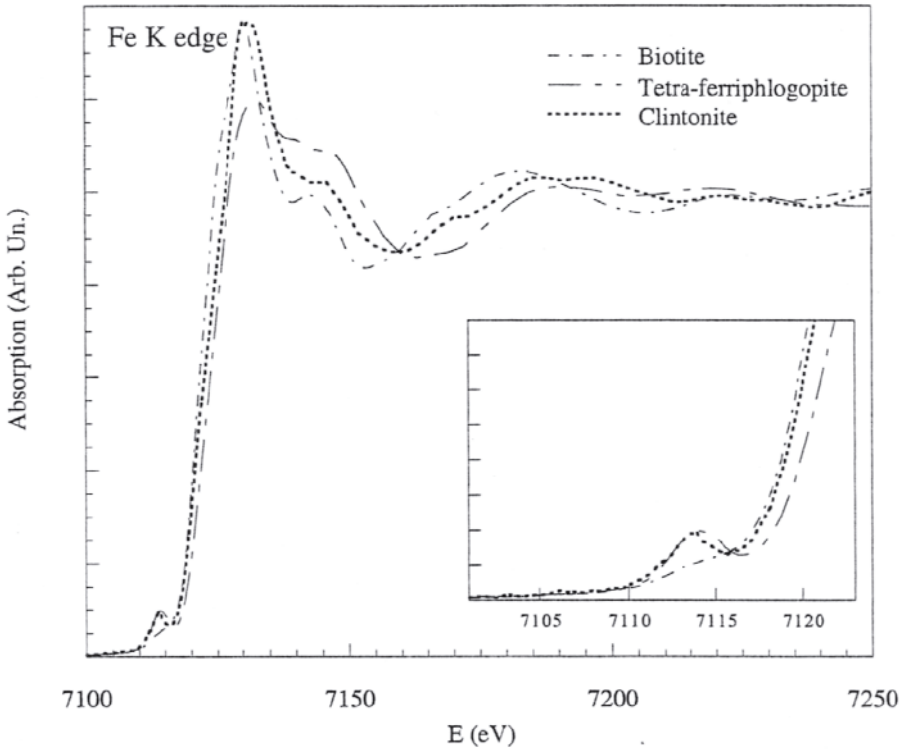

Figure 25. Experimental Fe *K*-edge spectra for the powders of two natural trioctahedral micas and one natural brittle mica. The pre-edge regions are shown as inset.

REFERENCES

Bair RA, Goddard WA (1980) Ab initio studies of the X-ray absorption edge in Cu complexes. I. Atomic Cu^{2+} and Cu(II)Cl_2. Phys Rev (Condens Matt) B22:2767-2776

Bajt S, Sutton SR, Delaney JS (1994) Microanalysis of iron oxidation states in silicates and oxides using X-ray absorption near-edge structure (XANES). Geochim Cosmochim Acta 58:5209-5214

Bajt S, Sutton SR, Delaney JS (1995) Microanalysis of iron oxidation states in Earth and planetary materials. Physica B208&209:243-244

Balzarotti A, Comin F, Incoccia L, Piacentini M, Mobilio S, Savoia A (1980) *K*-edge absorption of titanium in the perovskites $SrTiO_3$, $BaTiO_3$, and TiO_2. Solid State Commun 35:145-149

Bassett WA, Brown GE Jr (1990) Synchrotron radiation in the Earth sciences. Ann Rev Earth Planet Sci 18:387-447

Belli M, Scafati A, Bianconi A, Mobilio S, Palladino L, Reale A, Burattini E (1980) X-ray absorption near-edge structures (XANES) in simple and complex Mn compounds. Solid State Commun 35:355-361

Benfatto M, Congiu Castellano A, Daniele A, Della Longa S (2001) MXAN: A new software procedure to perform geometrical fitting of experimental XANES spectra. J Synchrotron Rad 8:267-269

Benfatto M, Natoli CR, Brouder C, Pettifer RF, Ruiz Lopez MF (1989) Polarized curved wave EXAFS: Theory and application. Phys Rev B39:1936-1939

Benfatto M, Natoli CR, Bianconi A, Garcia J, Marcelli A, Fanfoni M, Davoli I (1986) Multiple scattering regime and higher order correlations in X-ray absorption spectra of liquid solutions. Phys Rev B34:5774-5781

Bianconi A (1988) XANES spectroscopy. *In* DC Koningsberger, R Prins (eds) X-ray Absorption: Principles, applications, techniques of EXAFS, SEXAFS, and XANES. Wiley, New York, p 573-662

Bianconi A, Dell'Ariccia M, Durham PJ, Pendry JB (1982) Multiple-scattering resonances and structural effects in the X-ray absorption near-edge spectra of FeII and FeIII hexacyanide complexes. Phys Rev B26:6502-6508

Bianconi A, Fritsch E, Calas G, Petiau J (1985) X-ray absorption near-edge structure of 3d transition elements in tetrahedral coordination. The effects of bond-length variation. Phys Rev B32:4292-4295

Bianconi A, Incoccia L, Stipcich S (1983) EXAFS and Near-edge Structure (Springer Ser Chem Phys Vol. 27). Berlin, Springer-Verlag

Blum L, Abruna HD, White J, Gordon JG II, Borges GL, Samant MG, Melroy OR (1986) Study of underpotentially deposited copper on gold by fluorescence detected surface EXAFS. J Chem Phys 85:6732-6738

Bonnin D, Calas G, Suquet H, Pezerat H (1985) Site occupancy of Fe^{3+} in Garfield nontronite: a spectroscopic study. Phys Chem Minerals 12:55-64

Borowski M, Bowron DT, De Panfilis S (1999) High-energy X-ray absorption spectroscopy at ESRF BM29. J Synchrotron Rad 6:179-181

Brigatti MF, Galli E, Medici L, Poppi L, Cibin G, Marcelli A, Mottana A (2001) Chromium-containing muscovite: crystal chemistry and XANES spectroscopy. Eur J Mineral 13:377-389

Brown GE Jr, Calas G, Waychunas GA, Petiau J (1988) X-ray absorption spectroscopy: Applications in Mineralogy and Geochemistry. Rev Mineral 18:431-512

Brown GE Jr, Farges F, Calas G (1995) X-ray scattering and X-ray absorption studies of silicate melts. Rev Mineral 32:317-410

Brown GE Jr, Keefer KD, Fenn PM (1978) Extended X-ray absorption fine structure (EXAFS): study of iron-bearing silicate glasses: iron coordination environment and oxidation state. Geol Soc Am Ann Meet Abstr Progr 10:373

Brown GE Jr, Parks GA (1989) Synchrotron-based X-ray absorption studies of cation environments in Earth materials. Rev Geophys 27:519-533

Brytov IA, Konashenok KI, Romashchenko YuN (1979) Crystallochemical effects on Al *K* and Si *K* emission and absorption spectra for silicate and aluminosilicate minerals. Geochem Int'l 16:142-154

Cabaret D, Joly Y, Renevier H, Natoli CR (1999) Pre-edge structure analysis of Ti *K*-edge polarized X-ray absorption spectra in TiO_2 by full-potential XANES calculations. J Synchrotron Rad 6:258-260

Cabaret D, Sainctavit P, Ildefonse Ph, Flank A-M (1996) Full multiple-scattering calculations on silicates and oxides at the Al K edge. J Phys: Condens Matt 8:3691-3704

Calas G, Brown GE Jr, Waychunas GA, Petiau J (1984) X-ray absorption spectroscopic studies of silicate glasses and minerals. Phys Chem Minerals 15:19-29

Calas G, Levitz P, Petiau J, Bondot P, Loupias G (1980) Ètude de l'ordre local autour du fer dans les verres silicatés naturels et synthétiques à l'aide de la spectrométrie d'absorption X. Rev Phys Appl 15: 1161-1167

Calas G, Manceau A, Novikoff A, Boukili H (1984) Comportement du chrome dans les minéraux d'altération du gisement de Campo Formoso (Bahia, Brésil). Bull Minéral 107:755-766

Calas G, Petiau J (1983) Coordination of iron in oxide glasses through high-resolution *K*-edge spectra: information from the pre-edge. Solid State Commun 48:625-629

Cerino J, Stöhr J, Hower N, Bachrach R (1984) An ultra-high-vacuum double crystal monochromator beam line for studies in the spectral range 500-4000 eV. Nucl Instr Meth Phys Res 172:227-236

Chaboy J, Marcelli A, Tyson TA (1994) Influence of double-electron transitions on the EXAFS I edges of rare-earth systems. Phys Rev B49:11652-11661

Cibin G, Marcelli A, Mottana A (2001) Polarised X-ray absorption spectra at the Al *K* edge in Na^+ β- and β"-aluminas. Europhys Lett (submitted)

Clementi E, Roetti C (1974) Roothan-Hartree-Fock atomic wavefunctions. *In* Atomic Data and Nuclear Data Tables 14:177-478. Academic Press, New York

Cressey G, Henderson CMB, van der Laan G (1993) Use of *L*-edge X-ray absorption spectroscopy to characterize multiple valence states of 3d transition metals; a new probe for mineralogical and geochemical research. Phys Chem Minerals 20:111-119

Cruciani G, Zanazzi PF, Quartieri S (1995) Tetrahedral ferric iron in phlogopite: XANES and Mössbauer compared to single-crystal X-ray data. Eur J Mineral 7:255-265

Dartyge E, Fontaine A, Tourillon G, Cortes R, Jucha A (1986) X-ray absorption spectroscopy in dispersive mode and by total reflection. Phys Lett 113A:384-388

Davoli I, Paris E (1990) Principles and recent developments of XANES spectroscopy. *In* A Mottana, F Burragato (eds) Absorption Spectroscopy in Mineralogy. Elsevier, Amsterdam, p 206-226

Dehmer JL, Dill D (1976) Molecular effects on inner-shell photoabsorption. *K*-shell spectrum of N_2. J Chem Phys 65:5327-5334

Delaney JS, Sutton SR, Newville M, Jones JH, Hanson B, Dyar MD, Schreiber H (2000) Synchrotron micro-XANES measurements of vanadium oxidation state in glasses as a function of oxygen fugacity:

experimental calibration of data relevant to partition coefficient determination. 31st Ann Lunar Planet Sci Confe

Dell'Ariccia M, Gargano A, Natoli CR, Bianconi A (1984) A calculation of C *K*-shell X-ray absorption spectra of C_2H_n (n = 2, 4, 6) oriented molecules: correlation between position of the multiple scattering resonance in the continuum and the C-C bond length. LNF-INFN Report LNF-84-51 (P)

Deutsch M, Hart M (1984) Single X-ray photon excitation of two and three electrons in nickel. Phys Rev A29: 2946-2948

Díaz-Moreno S, Muñoz-Páez A, Chaboy J (2000) X-ray absorption spectroscopy (XAS) study of the hydratation structure of yttrium(III) cations in liquid and glassy states: eight or nine-fold coordination? J Phys Chem A2000:1278-1286

Doyle CS, Traina SJ, Ruppert H, Kandelewicz T, Rehr JJ, Brown GE Jr (1999) XANES studies at the Al *K*-edge of aluminum-rich surface phases in the soil environment. J Synchrotron Rad 6:621-623

Dräger G, Frahm R, Materlik G, Brümmer O (1988) On the multiplet character of the X-ray transitions in the pre-edge structure of Fe K absorption spectra. Phys Status Solidi 146:287-294

Drits VA, Dainyak LG, Muller F, Besson G, Manceau A (1997) Isomorphous cation distribution in celadonites, glauconites and Fe-illites determined by infrared, Mössbauer and EXAFS spectroscopies. Clay Minerals 32:153-179

Drozdov YuN, Klyuenkov EB, Lentovskaya NE, Mazo LA, Suslov LA (1997) Fullerene C60 layers on mica and sapphire. Poverkhnost (3):8-13 528

Durham PJ, Pendry JB, Hodges VH (1982) Calculation of X-ray absorption spectra based on the multiple scattering theory. Comput Phys Commun 25:193-205

Dyar MD, Delaney JS, Sutton SR (2000) Advances in interpretation of Fe XANES pre-edge spectra, and resultant improvements in microanalysis of ferric/ferrous ratios on thin sections. 31st Ann Lunar Planet Sci Conf

Dyar MD, Delaney JS, Sutton SR (2001) Fe XANES spectra of iron-rich micas. Eur J Mineral 13: 1079-1098

Dyar MD, McCammon C, Schaefer MW (eds) (1996) Mineral Spectroscopy: A Tribute to Roger G. Burns. Geochem Soc Spec Publ No. 5, 465 p

Filipponi A, Di Cicco A (2000) GNXAS: a software package for advanced EXAFS multiple-scattering calculations and data-analysis. Task Quarterly 4:575-669

Filipponi A, Di Cicco A, Benfatto M, Natoli CR (1990) The three-body correlation function in amorphous silicon probed by X-ray absorption spectroscopy. Europhys Lett 13:319-325

Filipponi A, Di Cicco A, Tyson TA, Natoli CR (1991) Ab initio modeling of X-ray absorption spectra. Solid State Commun 78:265-275

Filipponi A, Evangelisti F, Bernieri E, Mobilio S (1987) Double-electron excitation at the Si *K*-edge of amorphous silicon. J Phys Colloq 48, C9:961-964

Fricke H (1920) *K*-characteristic absorption frequencies for the chemical elements magnesium to chromium. Phys Rev 16:202-215

Fuhrmann M, Bajt S, Schoonen MAA (1998) Sorption of iodine on minerals investigated by X-ray absorption near-edge structure (XANES) and ^{125}I tracer sorption experiments. Appl Geochem 13: 127-141

Galoisy L, Calas G, Arrio MA (2001) High-resolution XANES spectra of iron in minerals and glasses: structural information from the pre-edge region. Chem Geol 174:307-319

Garcia J, Benfatto M, Natoli CR, Bianconi A, Davoli I, Marcelli A (1986) Three particle correlation function of metal ions in tetrahedral coordination determined by XANES. Solid State Commun 58:595-599

Giuli G, Paris E, Wu ZY, Brigatti MF, Cibin G, Mottana A, Marcelli A (2001) Experimental and theoretical XANES and EXAFS study of tetra-ferriphlogopite. Eur J Mineral 13 (in press)

Greaves GN, Durham PJ, Diakun G, Quinn P, Hart M, Siddons DP (1983) An order-sorting monochromator for synchrotron radiation. Nucl Instr Meth Phys Res 208:335-339

Gudat W, Kunz C (1972) Close similarity between photoelectric yield and photoabsorption spectra in the soft-X-ray range. Phys Rev Lett 29:169-172

Gurman SJ (1989) Structural information in extended X-ray absorption fine structure (EXAFS).*In* SS Hasnain (ed) Synchrotron Radiation and Biophysics. Ellis Horwood, Chichester, UK, p 9-42

Guttler B, Niemann W, Redfern SAT (1989) EXAFS and XANES spectroscopy study of the oxidation and deprotonation of biotite. Mineral Mag 53:591-602

Hahn JE, Scott RA, Hodgson KO, Doniach S, Desjardins SE, Solomon EI (1982) Observation of an electric quadrupole transition in the X-ray absorption spectrum of a Cu(II) complex. Chem Phys Lett 88: 595-598

Han Y-S, Choi S-H, Kim D-K (2001) Ion exchange and fixation of rare-earth cation into expandable tetrasilicic fluorine mica. J Synchrotron Rad 8:731-733

Hasnain SS (1989) Synchrotron Radiation and Biophysics. Ellis Horwood, Chichester, UK, 368 p
Hasnain SS (1991) X-ray Absorption Fine Structure. Ellis Horwood, Chichester, UK, 792 p
Hawthorne FC (ed) (1988) Spectroscopic methods in Mineralogy and Geology. Rev Mineral 18, 698 pp
Hayes TM, Boyces JB (1982) Extended X-ray absorption fine structure. Solid State Phys 37:173-351
Heald SM, Amonette JE, Turner GD, Scott AD (1995) An XAFS study of the oxidation of structural iron in biotite mica by solutions containing Br_2 or H_2O_2. Physica B208&209:604-606
Heald SM, Stern EA (1977) Anisotropic X-ray absorption in layered compounds. Phys Rev B16:5549-5559
Hedin L, Lundqvist BI (1971) Explicit local exchange-correlation potentials. J Phys C4:2064-2083
Henderson CMB, Charnock JM, Helz GR, Kohn SC, Patrick RAD, Vaughan DJ (1991) EXAFS in Earth science research. *In* SS Hasnain (ed) X-ray Absorption Fine Structure. Ellis Horwood, Chichester, UK, p 573-578
Hertz G (1920) Über Absorptionslinien im Röntgenspektrum. Physik Z 21:630-632
Holmes DJ, Batchelor DR, King DA (1988) Surface structure determination by SEXAFS: The reliability of bond lengths and coordination numbers from multi-shell analyses. Surface Sci 230:476-492
Huggins FE, Huffman GP (1996) Application of XAFS spectroscopy to coal geochemistry. *In* MD Dyar, C McCammon, MW Schaefer (eds) Mineral Spectroscopy: A tribute to Roger G. Burns. Geochem Soc Spec Publ No. 5:11-23
Hussain Z, Umbach E, Shirley DA, Stöhr J, Feldhaus J (1982) Performance and application of a double crystal monochromator in the energy region $800<h\nu<4500$ eV. Nucl Instr Meth Phys Res 195:115-131
Ildefonse Ph, Sainctavit P, Calas G, Flank A-M, Lagarde P (1998) Aluminum X-ray absorption near-edge structure in model compounds and Earth surface minerals. Phys Chem Minerals 25:112-121
Ildefonse Ph, Kirkpatrick RJ, Montez B, Calas G, Flank A-M, Lagarde P (1994) ^{27}Al MAS NMR and aluminum X-ray absorption near-edge structure of imogolites and allophanes. Clays Clay Minerals 42:276-287
Jagannatha Rao B, Chetal AR (1982) An X-ray *K*-absorption study of muscovite mica. J Phys D: Appl Phys 15:L195-L197
Jain DC, Chandra U, Garg KB, Sharma BK (1980) X-ray absorption study of some iron-rich micas. J Phys D: Appl Phys 13:1113-1120
Johnson KH (1966) Multiple-scattering model for polyatomic molecules. J Chem Phys 45:3085-3095
Johnson KH (1973) Scattered-wave theory of the chemical bond. Adv Quantum Chem 7:143-185
Joly Y (2001) X-ray absorption near-edge structure calculations beyond the muffin-tin approximation. Phys Rev B63:125120-1-10
Joly Y, Cabaret D, Renevier H, Natoli CR (1999) Electron population analysis by full-potential X-ray absorption simulations. Phys Rev Lett 82:2398-2401
Kaiser P, Bonnin D, Frétigny C, Cortes R, Manceau A (1989) Ètude EXAFS en polarisation de composés lamellaires. J Chim Phys 86:1699-1706
Kaulich B, Barrett R, Salomé M, Oestreich S, Susini J (2000) X-ray imaging with sub-100-nm spatial resolution at 4 KeV. ESRF Newsletter 34:27-28
Kemner KM, Hunter DB, Bertsch PM, Kirkland JP, Elam WT (1997) Determination of site specific binding environments of surface sorbed cesium on clay minerals by Cs-EXAFS. J Phys IV 7, Colloq 2, Supp J Phys III d'Avril 1997, C2:777-779
Kincaid BM, Eisenberger P (1975) Synchrotron radiation study of the *K*-edge photoabsorption spectra of Kr, Br_2 and $GeCl_4$: comparison of theory and experiment. Phys Rev Lett 34:1361-1364
Koch EE (1983) Handbook on Synchrotron Radiation (Vol. 1b). North-Holland, New York, 506 p
Koningsberger DC, Prins R (1988) X-ray absorption: Principles, Applications, Techniques of EXAFS, SEXAFS, and XANES. Wiley, New York, 673 p
Kossel W (1920) Zum Bau der Röntgenspektren. Z Phys 1:119-134
Kronig RL (1931) Zur Theorie der Feinstruktur in den Röntgenabsorptionsspektren. Z Phys 70:317-323
Kronig RL (1932a) Zur Theorie der Feinstruktur in den Röntgenabsorptionsspektren. II. Z Phys 75:191-210
Kronig RL (1932b) Zur Theorie der Feinstruktur in den Röntgenabsorptionsspektren. III. Z Phys 75: 468-475
Kutzler FW, Natoli CR, Misemer DK, Doniach S, Hodgson KO (1980) Use of one electron theory for the interpretation of near-edge structure in *K*-shell X-ray absorption spectra of transition metal complexes. J Chem Phys 73:3274-3288
Kuzmin A, Parent Ph (1994) Focusing and superfocusing effects in X-ray absorption fine structure at the iron K edge in FeF_3. J Phys: Conden Matt 6:4395-4404
Kuzmin A, Purans J, Parent Ph (1995) Influence of the focusing effect on XAFS in ReO_3, WO_{3-x} and FeF_3. Physica B208&209:45-46
Lee JF, Bajt S, Clark SB, Lamble GM, Langton CA, Oji L (1995) Chromium speciation in hazardous, cement-based waste forms. Physica B208 and 209:577-578

Lee PA, Beni G (1977) New method for the calculation of atomic phase shifts: applications to extended X-ray absorption fine structure (EXAFS) in molecules and crystals. Phys Rev B15:2862-2883

Lee PA, Citrin PH, Eisenberger P, Kincaid BM (1981) Extended X-ray fine structure: Its strength and limitations as a structural tool. Rev Modern Phys 53:769-806

Lee PA, Pendry JB (1975) Theory of extended X-ray absorption fine structure. Phys Rev B11:2795-2811

Li D, Bancroft, GM Fleet, ME Feng, XH (1995a) Silicon *K*-edges XANES spectra of silicate minerals. Phys Chem Minerals 22:115-122

Li D, Bancroft GM, Fleet ME, Feng XH, Pan Y (1995b) Al *K*-edge XANES spectra of aluminosilicate minerals. Am Mineral 80:432-440

Li D, Bancroft GM, Kasrai M, Fleet ME, Secco RA, Feng XH, Tan KH, Yang BX (1994) X-ray absorption spectroscopy of silicon dioxide (SiO_2) polymorphs: The structural characterization of opal. Am Mineral 79:622-632

Lytle FW (1989) Experimental X-ray absorption spectroscopy; pp. 135-223 *In* H Winick, D Xian, M Ye, T Huang (eds) Applications of synchrotron radiation. Gordon and Breach, New York

Lytle FW (1999) The EXAFS family tree: a personal history of the development of extended X-ray absorption fine structure. J Synchrotron Rad 6:123-134

Manceau A (1990) Distribution of cations among the octahedra of phyllosilicates: Insight from EXAFS. Can Mineral 28:321-328

Manceau A, Bonnin D, Kaiser P, Frétigny C (1988) Polarized EXAFS of biotite and chlorite. Phys Chem Minerals 16:180-185

Manceau A, Bonnin D, Stone WEE, Sanz J (1990) Distribution of iron in the octahedral sheet of trioctahedral micas by polarized EXAFS. Comparison with NMR results. Phys Chem Minerals 17: 363-370

Manceau A, Calas G (1986) Nickel-bearing clay minerals: II. Intracrystalline distribution of nickel: an X-ray absorption study. Clay Minerals 21:341-360

Manceau A, Chateigner D, Gates WP (1998) Polarized EXAFS, distance-valence least-squares modeling (DVLS) and quantitative texture analysis approaches to the structural refinement of Garfield nontronite. Phys Chem Minerals 25:347-365

Mottana A, Burragato F (1990) Absorption Spectroscopy in Mineralogy. Elsevier, Amsterdam-Oxford-New York-Tokyo, 294 p

Mottana A, Murata T, Wu ZY, Marcelli A, Paris E (1997) The local structure of Ca-Na pyroxenes. I. XANES study at the Na *K*-edge. Phys Chem Minerals 24:500-509

Mottana A, Murata T, Wu ZY, Marcelli A, Paris E (1999) The local structure of Ca-Na pyroxenes. II. XANES studies at the Mg and Al *K*-edges. Phys Chem Minerals 27:20-33

Mottana A, Robert J-L, Marcelli A, Giuli G, Della Ventura G, Paris E, Wu Z (1997) Octahedral versus tetrahedral coordination of Al in synthetic micas determined by XANES. Am Mineral 82:497-502

Müller JE, Jepsen O, Wilkins JW (1982) X-ray absorption spectra: *K*-edges of 3d transition metals, *I*-edges of 3d and 4d metals, and *M*-edges of palladium. Solid State Commun 42:365-368

Müller JE, Wilkins JW (1984) Band-structure approach to the X-ray spectra of metals. Phys Rev B29: 4331-4348

Natoli CR (1983) Near-edge absorption structure in the framework of the multiple scattering model. Potential resonance on barrier effects. *In* A Bianconi, L Incoccia, S Stipcich (eds) EXAFS and Near-edge Structure. Springer Ser Chem Phys 27:43-47

Natoli CR (1985) Distance dependence of continuum and bound state of excitonic resonances in X-ray Absorption Near-edge Structure (XANES). *In* KO Hodgson, B Hedman and JE Penner-Hahn (eds) EXAFS and Near-edge Structure III (Springer Proceed Phys). Berlin, Springer-Verlag, p 38-42

Natoli CR, Benfatto M (1986) A unifying scheme of interpretation of X-ray absorption spectra based on multiple scattering theory. *In* P Lagarde, D Raoux, J Petiau (eds) EXAFS and Near-Edge Structure IV. J Phys 47-C8, p 11-23

Natoli CR, Benfatto M, Brouder C, Ruiz Lopez MZ, Foulis DL (1990) Multichannel multiple-scattering theory with general potentials. Phys Rev B42:1944-1968

Natoli CR, Benfatto M, Doniach S (1986) Use of general potentials in multiple scattering theory. Phys Rev A34:4682-4694

Natoli CR, Misemer DK, Doniach S, Kutzler FW (1980) First-principles calculation of X-ray absorption-edge structure in molecular cluster. Phys Rev B22:1104-1108

Obashi, M (1978) X-ray Fe K absorption edges of $[Fe(CN)_6]^{4-}$ and $Fe(CN)_6]^{3-}$. Japan J Appl Phys 17: 563-566

Ohta T, Takeda H, Takéuchi Y (1982) Mica polymorphism: Similarities in the crystal structures of coexisting 1M and $2M_1$ oxybiotite. Am Mineral 67:298-310

Osuka T, Morikawa H, Marumo F, Daimon N, Udagawa Y, Toji K (1988) An EXAFS study of local structures around cobalt atoms in synthetic fluormicas. Rep Res Lab Engineer Mater, Tokyo Inst Techn 13:1-6

Osuka T, Shimizugawa Y, Morikawa H, Marumo F, Udagawa Y, Tohji K (1990) An EXAFS study of coordination of Mn atoms in synthetic manganoan fluormicas [in Japanese, English abstr]. Kobutsugaku Zasshi 19:209-218

Paris E, Mottana A, Mattias P (1991) Iron environment in a montmorillonite from Gola del Furlo (Marche, Italy). A synchrotron radiation XANES and a Mössbauer study. Mineral Petrol 45:105-117

Pendry JB (1983) X-ray absorption near-edge structure. Comments Solid State Phys 10:219-231

Peterson ML, Brown GE Jr, Parks GA, Stein CL (1997) Differential redox and sorption of Cr(III/VI) on natural silicate and oxide minerals: EXAFS and XANES results. Geochim Cosmochim Acta 61: 3399-3412

Petit P-E, Farges F, Wilke M, Solé VA (2001) Determination of the iron oxidation state in Earth materials using XANES pre-edge information. J Synchrotron Rad 8:952-954

Pettifer RF, Brouder C, Benfatto M, Natoli CR, Hermes C, Ruiz López MF (1990) Magic-angle theorem in powder X-ray-absorption spectroscopy. Phys Rev B42:37-42

Phizackerley RP, Rek ZU, Stephenson GB, Conradson SD, Hodgson KO, Matsushita T, Oyanagi H (1983) An energy-dispersive spectrometer for the rapid measurement of X-ray absorption spectra using synchrotron radiation. J Applied Crystallogr 16:220-232

Randall CR, Shu L, Chiou Y-M, Hagen KS, Ito M, Kitajima N, Lachicotte RJ, Zang Y, Que L (1995) X-ray absorption pre-edge studies of high-spin iron(II) complexes. Inorg Chem 34:1036-1039

Ravel B, Stern EA, Yacobi Y, Dogan J (1993) Ti lead titanate is not a classic case of a displacive ferro-electric phase-transition. Japan J Applied Phys Supp 32-2:782-784

Rehr JJ, Albers RC (2000) Theoretical approaches to X-ray absorption fine structure. Rev Modern Phys 72:621-654

Rehr JJ, Zabinsky ZI, Albers RC (1992) Higher-order multiple scattering calculations of X-ray-absorption fine structure. Phys Rev Lett 69:3397-4000

Rickwood PC (1981) The largest crystals. Am Mineral 66:885-907

Rieder M, Cavazzini G, D'yakonov YuS, Frank-Kamenetskii VA, Gottardi G, Guggenheim S, Koval' PV, Müller G, Neiva AMR, Radoslovich EW, Robert J-L, Sassi FP, Takeda H, Weiss Z, Wones DR (1998) Nomenclature of the micas. Can Mineral 36:905-912

Roe AL, Schneider DJ, Mayer RJ, Pyrz JW, Widom J, Que L Jr (1984) X-ray absorption spectroscopy of iron-tyrosinate proteins. J Am Chem Soc 106:1676-1681

Ruiz-López MF, Muñoz-Páez AM (1991) A theoretical study of the XANES spectra of rutile and anatase. J Phys: Condens Matter 3:8981-8990

Sakane H, Okabe M-O, Suzuki T (1997) Local structure of the interlayer ion in synthetic fluorine mica. J Phys IV 7, Colloque 2, Supplément J Physique III d'Avril 1997, C2:1165-1166

Sayers DE, Lytle FW, Stern EA (1970) Point scattering theory of X-ray K absorption fine structure. Adv X-ray Anal 13:248-271

Sayers DE, Stern EA, Lytle FW (1971) New technique for investigating noncrystalline structures: Fourier analysis of the extended X-ray absorption fine structure. Phys Rev Lett 27:1204-1207

Schaefers F, Müller BR, Wong J, Tanaka T, Kamimura Y (1992) YB_{66}: a new soft X-ray monochromator crystal. Synchrotron Rad News 5[2]:28-30

Schofield PF, Henderson CMB, Cressey G, van der Laan G (1995) 2p X-ray absorption spectroscopy in the Earth sciences. J Synchrotron Rad 2:93-98

Shulman RG, Yafet Y, Eisenberger P, Blumberg WE (1976) Observation and interpretation of X-ray absorption edges in iron compounds and proteins. Proc Nat'l Acad Sci 73:1384-1388

Slater JC (1979) Quantum Theory of Molecules and Solids. New York, McGraw-Hill, 467 p

Soma M, Tanaka A, Seyama H, Hayashi S, Hayamizu K (1990) Bonding states of sodium in tetrasilicic sodium fluor mica. Clay Sci 8:1-8

Spiro C, Wong J, Maylotte DH, Lamson S, Glover B, Lytle FW, Greegor RB (1984) Nature of potassium impurities in coal; pp. 368-370 *In* KO Hodgson, B Hedman, JE Penner-Hahn (eds) EXAFS and near-edgeedge structure III (Springer Proc Phys). Berlin, Springer-Verlag

Stebbins JF, McMillan PF, Dingwell DB (1995) Structure, dynamics and properties of silicate melts. Rev Mineral 32, 616 p

Stern EA (1974) Theory of extended X-ray absorption fine structure. Phys Rev B10:3027-3037

Stern EA, Heald SM (1983) Basic principles and applications of EXAFS; pp. 955-1014 *In* EE Koch (ed) Handbook on Synchrotron Radiation (Vol. 1b). North-Holland, New York

Stöhr J, Jaeger R, Feldhaus J, Brennan S, Norman D, Apai G (1980) Extended absorption fine structure studies above the carbon, nitrogen, oxygen, and fluorine *K* absorption edges. Appl Optics 19: 3911-3919

Stöhr J, Noguera C, Kendelewicz T (1984) Auger and photoelectron contributions to the electron-yield surface extended X-ray-absorption fine-structure signal. Phys Rev B30:5571-5579

Sutton SR, Bajt S, Delaney J, Schulze D, Tokunaga T (1995) Synchrotron X-ray fluorescence microprobe: Quantification and mapping of mixed valence state samples using micro-XANES. Rev Sci Instrum 66:1464-1467

Teo BK (1986) EXAFS: Basic Principles and Data Analysis (Inorganic Chemistry Concepts 9). Springer-Verlag, Berlin, 349 p

Teo BK, Lee PA (1979) Ab initio calculation of amplitude and phase function for extended X-ray absorption fine structure (EXAFS) spectroscopy. J Am Chem Soc 101:2815-2830

Teo BK, Simons AL, Eisenberger P, Kincaid BM (1977) EXAFS: approximations, parameterization, and chemical transferability of amplitude functions. J Am Chem Soc 99:3854-3856

Tyson TA, Hodgson KO, Natoli CR, Benfatto M (1992) General multiple-scattering scheme for the computation and interpretation of X-ray-absorption fine structure in atomic clusters with applications to SF_6, $GeCl_4$, and Br_2 molecules. Phys Rev B46:5997-6019

Uozumi T, Okada K, Kotani A, Durmeyer O, Kappler JP, Beaurepaire E, Parlebas JC (1992) Experimental and theoretical investigation of the pre-peaks at the Ti *K*-edge absorption spectra in TiO_2. Europhys Lett 18:85-90

Vedrinskii RV, Kraizman VL, Novakovich AA, Demekhin PhV, Urazhdin SV, Ravel B, Stern EA (1997) Pre-edge fine structure (PEFS) of the *K*-XAS for the 3d atoms in compounds: A new tool for quantitative atomic structure determination. J Phys IV 7, Colloq 2, Supp J Phys III d'Avril 1997, C2:107-110

Waychunas GA (1987) Synchrotron radiation XANES spectroscopy of Ti in minerals: Effects of Ti bonding distances, Ti valence, and site geometry on absorption edge structure. Am Mineral 72:89-101

Waychunas GA, Apted MJ, Brown GE Jr (1983) X-ray *K*-edge absorption spectra of Fe minerals and model compounds: I. Near-edge structure. Phys Chem Minerals 10:1-9

Waychunas GA, Brown GE Jr, Apted MJ (1986) X-ray *K*-edge absorption spectra of Fe minerals and model compounds: II. EXAFS. Phys Chem Minerals 13:31-47

Westre TE, Kennepohl P, DeWitt JG, Hedman B, Hodgson KO, Solomon EI (1997) A multiplet analysis of Fe *K*-edge 1s-3d pre-edge features of iron complexes. J Am Chem Soc 119:6297-6314

Winick H, Xian D, Ye M, Huang T (1989) Applications of synchrotron radiation (Proc CCAST Symp, June 1988, Beijing. Ser Part: China Center Adv Sci Technol Series, Vol. 4). Gordon and Breach, New York, 626 p

Wong J, Lytle FW, Messmer RP, Maylotte DH (1984) A study of the *K*-edge absorption spectra of selected vanadium compounds. Phys Rev B30:5596-5610

Wong J, Rek ZU, Rowen M, Tanaka T, Schaefers F, Müller B, George GN, Pickering IJ, Via G, DeVries B, Brown GE Jr, Fröba M (1995) New opportunities in 1-2 keV spectroscopy. Physica B208&209:220-222

Wong J, Shimkaveg G, Goldstein W, Eckart M, Tanaka T, Rek ZU, Tompkins H (1990) YB_{66}: A new soft-X-ray monochromator for synchrotron radiation. Nucl Instr Methods Phys Res A291:243-249

Wong J, Tanaka T, Rowen M, Schäfers F, Müller BR, Rek ZU (1999) YB_{66}—A new soft-X-ray monochromator for synchrotron radiation. II. J Synchrotron Rad 6:1086-1095

Wu ZY, Marcelli A, Mottana A, Giuli G, Paris E, Seifert F (1996) Effects of higher-coordination shells in garnets detected by XAS at the Al *K*-edge. Phys Rev B54:2976-2979

Zabinsky SI, Rehr JJ, Ankudinov A, Albers RC, Eller MJ (1995) Multiple scattering calculations of X-ray absorption spectra. Phys Rev B52:2995-3006